Anthropogenic climate change for 1860 to 2100 simulated with the HadCM3 model under updated emissions scenarios

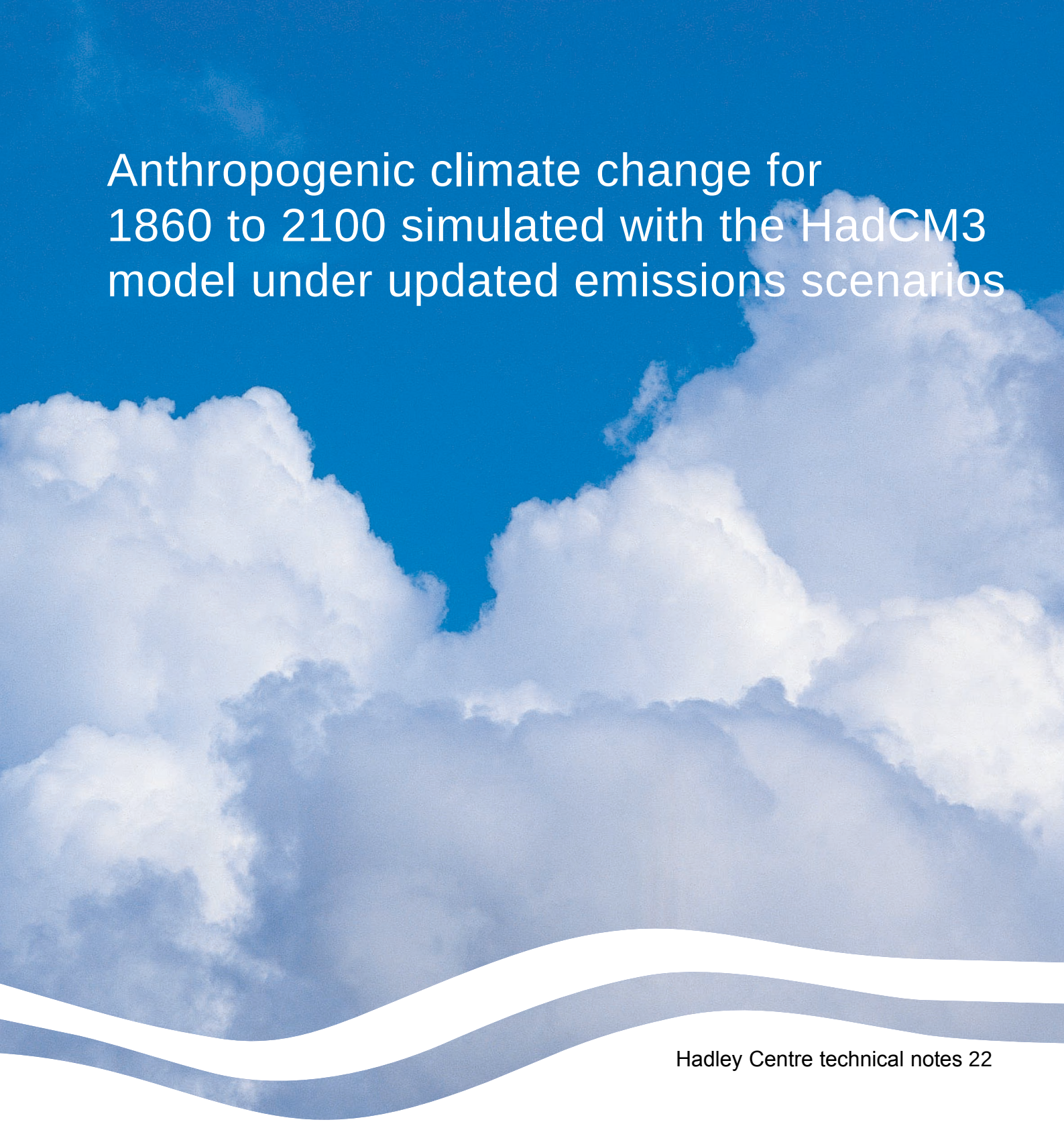

Hadley Centre technical notes 22

T.C. Johns, J.M. Gregory, W.J. Ingram, C.E. Johnson, A. Jones, J.A. Lowe, J.F.B. Mitchell, D.L. Roberts, D.M.H. Sexton, D.S. Stevenson, S.F.B. Tett, and M.J. Woodage

24 January 2001

Met Office

Anthropogenic climate change for 1860 to 2100 simulated with the HadCM3 model under updated emissions scenarios

T.C. Johns, J.M. Gregory, W.J. Ingram, C.E. Johnson, A. Jones, J.A. Lowe, J.F.B. Mitchell, D.L. Roberts, D.M.H. Sexton, D.S. Stevenson*, S.F.B. Tett, and M.J. Woodage

Met Office, Hadley Centre for Climate Prediction and Research, London Road, Bracknell, RG12 2SY

* - Now at Department of Meteorology, University of Edinburgh King's Buildings, Edinburgh EH9 3JZ

Hadley Centre Technical Note No. 22

24 Jan 2001

Corresponding author's address:

Dr. Tim Johns,
Met Office,
Hadley Centre for Climate Prediction and Research,
London Road,
Bracknell,
RG12 2SY,
UK
tel: +[44]-1344-856901
fax: +[44]-1344-854898
email: tcjohns@meto.gov.uk

Abstract

We present results from a climate model study designed to evaluate the forced response to anthropogenic emissions over the historical period from 1860 to the present, and the projected climate change response up to 2100, using updated scenarios and an improved modelling methodology. We concentrate on the new marker scenarios A1FI, A2 and B2 from the Special Report on Emissions Scenarios (SRES) prepared for the IPCC Third Assessment Report, since these are more self-consistent in their socio-economic, population, energy-use and resulting emissions structure than older scenarios like IS92a. This makes the model results more directly relevant to policymakers. The climate model used, HadCM3, is an improved version of the Hadley Centre coupled model and produces a realistic and stable climate simulation without flux adjustments. Our modelling methodology now includes an interactive representation of the anthropogenic sulphur cycle and both direct and indirect radiative forcings from sulphate aerosols applied in a physically plausible way. We also model scenario-related variations in tropospheric and stratospheric ozone, although the chemistry-climate feedbacks for ozone are not yet fully interactive. The natural component of the sulphur cycle is not included explicitly in the climate change simulations, although it is employed in related off-line calibrations of the indirect sulphate forcing. Evaluation of the model results suggests that the sulphate burdens are lower than observational estimates, giving a low value for the direct effect. The sulphate forcing due to the first indirect effect through cloud droplet size is considerably stronger. The implied low background atmospheric sulphate burden will enhance the anthropogenic indirect sulphate forcing, but it is not clear whether this will be enough to compensate for the underestimate of the direct effect. We have not yet considered the second indirect sulphate aerosol forcing effect through cloud lifetimes, which would increase the total negative forcing if included. Considering the greenhouse gas (GHG) forced response only, climate changes in B2 are similar in pattern to IS92a but somewhat smaller in magnitude. Inclusion of sulphate and ozone forcing substantially modulates the response, tending to cool the land particularly in northern mid-latitudes, and altering the monsoonal structure. By 2100, the global-mean warming in the new scenarios ranges from 2.9 to 5.2 K warmer than 1900. Global-mean precipitation increases by about 1%/K through the 21st century (1.4%/K when changes in aerosol are omitted). The large-scale patterns of change generally resemble those found in an earlier model (HadCM2), but with several notable exceptions. HadCM2 gave a secondary maximum warming in the tropics associated with a local enhancement of precipitation in the Inter-Tropical Convergence Zone (ITCZ), whereas in the new model the warming increases monotonically from south to north across the equator, and the ITCZ shifts northward. The new model also produces a larger increase in precipitation in the Asian south west monsoon, and a more uniform drying of the land surface over the northern mid-latitude continents in summer. The mid-USA region exhibits a large projected global warming, up to 6.6 K warmer than the present day towards the end of the 21st century. Precipitation changes are not all consistent across the five

scenarios for the five regions analysed in detail, but robust signals include marked drying in the mid-USA and southern Europe and significantly wetter conditions developing in South Asia, in June to August, with likely consequences for incidence of drought and floods.

1 Introduction

There is growing expectation that increases in the concentrations of greenhouse gases arising from human activity will lead to significant and substantial changes in climate in the 21st century. Indeed, there is already evidence that anthropogenic emissions of greenhouse gases (GHGs) have altered the large scale patterns of temperature over the 20th century [*Santer et al.,* 1996; *Tett et al.,* 1999; *Barnett,* 1999; *Stott et al.,* 2001], although natural factors, including changes in solar output and episodic volcanic emissions, may also have contributed. Future climate change will probably be dominated by the response to anthropogenic forcing factors. Large uncertainties remain, however, in the expected anthropogenic climate response, partly through model uncertainty in the projected climate sensitivity to increasing GHGs and partly as a result of both physical and modelling uncertainties in the amplitude and geographical patterns of non-GHG forcings which modulate this GHG-forced response (particularly from sulphate aerosol indirect cooling effects).

The main motivation for the present study is to provide up-to-date estimates of global climate change suitable for deriving impacts assessments on regional scales with self-consistent scenario assumptions. Even though some of the regional details may be unreliable, this approach at least gives a picture of possible consequences of alternative future emissions scenarios, derived in a physically consistent way, which can be interpreted for policymakers in the context of negotiations to limit emissions so as to prevent 'dangerous' climate change.

Some questions that arise are whether GHG-induced warming (determined by global average emissions) will dominate, or whether local sulphate aerosol forcing (much more dependent on local emissions) will be a significant factor over the 21st century and, if the latter, what differences in the regional responses might be expected under different emissions scenarios? Could non-linear climate-chemistry feedbacks become increasingly important to consider in future, with an implication of added importance attached to emissions pathways? To tackle such questions it is important that there should be consistency and some plausibility about the emissions scenarios used to force climate models. The IPCC SRES ('Special Report on Emissions Scenarios', *Nakicenovic et al.,* 2000) marker scenarios developed in conjunction with the IPCC Third Assessment Report, have been developed specifically to provide more self-consistent and up-to-date scenarios for climate modelling than hitherto. We have therefore primarily adopted these in the present study, though we also refer back to the older IS92a scenario which has already been used

extensively in climate impact studies (eg. [*US National Assessment Report,* 2000; *Hulme et al.,* 1999; *Hulme and Jenkins,* 1998]).

Given emission scenarios of GHGs, sulphur and other anthropogenic precursor gases, understanding the climate sensitivity to the resulting anthropogenic forcings and the interactions between climate change, atmospheric chemistry feedbacks and transport processes is still a major challenge. Coupled climate models including representations of the relevant physical, dynamical and chemical processes are an essential tool, not just for making predictions but for increasing understanding of the feedbacks and sensitivities. Here we use a state-of-the-art coupled climate model (HadCM3 - *Gordon et al.,* 2000) incorporating an explicit sulphur cycle to predict anthropogenic sulphate burdens from emissions and including the anthropogenic forcing effects thought to be most relevant at the moment, applied in a way as consistent with the emissions scenario as possible. The results therefore represent plausible estimates of global climate change consequent upon the socio-economic assumptions underlying the emissions scenarios.

The structure of this paper is as follows. In the next section we document the version of the coupled model used in the study and the physical basis for calculating the anthropogenic forcings. In Section 3 we briefly outline the performance of the model in a long control integration with no anthropogenic forcing imposed. Then in Section 4 we outline the anthropogenically-forced experiments, with a fuller description of the emissions, concentrations and forcing scenarios in Section 5. In Section 6 we examine the modelled future climate response and regional variations in the various forcing scenarios, assessing them in the light of previous model studies and exploring the questions posed above. Some final conclusions, caveats and future outlook are presented in Section 7.

2 Model description

The HadCM3 coupled model [*Gordon et al.,* 2000] is used in the simulations. HadCM3 was developed from the earlier HadCM2 model [*Johns et al.,* 1997], but various improvements to the atmosphere and ocean components mean that it needs no artificial flux adjustments to prevent excessive climate drift. The atmosphere and ocean exchange information once per day, heat and water fluxes being conserved exactly.

Atmosphere

The atmospheric component of the model, HadAM3 [*Pope et al.,* 2000], has 19 levels with a horizontal resolution of 2.5° latitude by 3.75° longitude, comparable to a spectral resolution of T42.

A new radiation scheme is included with 6 spectral bands in the shortwave and 8 in the longwave. The radiative effects of minor greenhouse gases as well as CO_2, water vapour and ozone are explicitly represented [*Edwards and Slingo,* 1996]. A simple parametrization of background aerosol [*Cusack et al.,* 1998] is also included.

A new land surface scheme [*Cox et al.,* 1999] includes a representation of the freezing and melting of soil moisture, as well as surface runoff and soil drainage; the formulation of evaporation includes the dependence of stomatal resistance on temperature, vapour pressure and CO_2 concentration. The surface albedo is a function of snow depth, vegetation type and also of temperature over snow and ice.

A penetrative convective scheme [*Gregory and Rowntree,* 1990] is used, modified to include an explicit downdraught and the direct impact of convection on momentum [*Gregory et al.,* 1997]. Parametrizations of orographic and gravity wave drag have been revised to model the effects of anisotropic orography, high drag states, flow blocking and trapped lee waves [*Milton and Wilson,* 1996; *Gregory et al.,* 1998]. The large-scale precipitation and cloud scheme is formulated in terms of an explicit cloud water variable following *Smith* [1990]. The effective radius of cloud droplets is a function of cloud water content and droplet number concentration [*Martin et al.,* 1994].

Ocean and sea ice

The oceanic component of the model has 20 levels with a horizontal resolution of 1.25° x 1.25°. At this resolution it is possible to represent important details in oceanic current structures [*Wood et al.,* 1999].

Horizontal mixing of tracers uses a version of the adiabatic diffusion scheme of *Gent and McWilliams* [1990] with a variable thickness diffusion parametrization [*Wright,* 1997; *Visbeck et al.,* 1997]. There is no explicit horizontal diffusion of tracers. The along-isopycnal diffusivity of tracers is 1000 m^2/s and horizontal momentum viscosity varies with latitude between 3000 and 6000 m^2/s at the poles and equator respectively.

Near-surface vertical mixing is parametrized by a Kraus-Turner mixed layer scheme for tracers [*Kraus and Turner,* 1967], and a K-theory scheme [*Pacanowski and Philander,* 1981] for momentum. Below the upper layers the vertical diffusivity is an increasing function of depth only. Convective adjustment is modified in the region of the Denmark Straits and Iceland-Scotland ridge better to represent down-slope mixing of the overflow water, which is allowed to find its proper level of neutral buoyancy rather than mixing vertically with surrounding water masses. The scheme is based on *Roether et al.* [1994].

Mediterranean water is partially mixed with Atlantic water across the Strait of Gibraltar as a simple representation of water mass exchange since the channel is not resolved in the model.

The sea ice model uses a simple thermodynamic scheme including leads and snow-cover. Ice is advected by the surface ocean current, with convergence prevented when the depth exceeds 4 m [*Cattle and Crossley,* 1995].

There is no explicit representation of iceberg calving, so a prescribed water flux is returned to the ocean at a rate calibrated to balance the net snowfall accumulation on the ice sheets, geographically distributed within regions where icebergs are found. In order to avoid a global average salinity drift, surface water fluxes are converted to surface salinity fluxes using a constant reference salinity of 35 PSU.

Sulphur cycle and sulphate aerosols

In addition to the above improvements in existing physical schemes, HadAM3 also now includes the capability to model the transport, chemistry and physical removal processes of anthropogenic sulphate aerosol which is input to the model in the form of surface and high level emissions of SO_2 (outlined below; a fuller description of the interactive sulphur cycle in the model may be found in *Jones et al.,* 1999). [Note that this is in contrast to some earlier climate model studies which only included sulphate aerosol effects based on prescribed burdens].

Sulphur dioxide (SO_2), dimethyl sulphide (DMS) and three modes of sulphate aerosol can be represented explicitly in terms of mass-mixing ratio as prognostic variables in HadAM3. There are two size modes of free sulphate particle, both assumed to have lognormal size distributions; the Aitken mode has median radius 24nm and geometric standard deviation $\sigma_{ait} = 1.45$, and the accumulation mode has median radius 95nm and $\sigma_{acc} = 1.4$. The third mode represents sulphate dissolved in cloud droplets. The variables are advected horizontally and vertically using a positive definite tracer advection scheme (distinct from the advection scheme used for the atmospheric prognostic variables), and also transported in the vertical by the convection scheme. Turbulent mixing in the boundary layer is parametrized in a way similar to that of heat and moisture, with the allowance for injection of SO_2 and DMS emissions at appropriate levels, and dry deposition of SO_2 and sulphate species at the surface. Sulphur is introduced into the model as emissions of SO_2 (anthropogenic or volcanic) or DMS. These are converted to the sulphate modes in a chemistry routine included in the model, which parametrizes the gas and aqueous phase oxidation reactions using monthly mean 3-dimensional oxidant fields (OH, H_2O_2 and HO_2) from the STOCHEM Lagrangian chemistry model [*Collins et al.,* 1997; *Collins et al.,* 1999], HO_2 being used to regenerate hydrogen peroxide. The oxidant distributions used

in the experiments described later were derived from a STOCHEM run appropriate for present day conditions [*Stevenson et al.,* 2000]. The following transfers between the sulphate modes are also parametrized: evaporation of dissolved sulphate to form accumulation mode, nucleation of accumulation mode sulphate to form dissolved sulphate, and diffusion of Aitken mode sulphate into cloud droplets. Wet scavenging of SO_2 and the sulphate modes is parametrized in the model's large-scale precipitation and convection schemes.

The Aitken and accumulation sulphate modes are used in the radiation code to simulate their direct effect on the Earth's radiation budget; that is, the direct scattering or absorption of incoming solar radiation by the aerosol particles. For this purpose, the particles are assumed to be composed of a mixture of ammonium sulphate and water, the refractive indices of ammonium sulphate at selected wavelengths being taken from *Toon et al.* [1976]. The particles are assumed to be spherical, so that Mie theory can be used to calculate the scattering and absorption coefficients. This is done separately for the Aitken and accumulation modes, which are assigned the lognormal size distributions as above. However these are the distributions of the dry particles; for radiative purposes the hygroscopic growth of the particles is taken into account so that their effective sizes are often larger, by an amount that depends on the relative humidity in the model. The growth function is based partly on the parametrization of *Fitzgerald* [1975], which has the convenient property that the size distribution of the moist aerosol continues to be lognormal. It should be noted that Mie theory calculations are not performed during the model integration, but beforehand; the results are supplied to the model in the form of look-up tables of aerosol single scattering parameters for both the Aitken and accumulation modes.

To estimate the indirect effect of sulphate aerosols on the radiative properties of clouds account must be taken of the fact that cloud droplet number concentrations (N_d) in the HadCM3 control run are set to fixed values of 600 cm^{-3} over land and 150 cm^{-3} over ocean [*Bower and Choularton,* 1992]. Another consideration is the fact that the HadCM3 experiments only consider anthropogenic SO_2 emissions. Consequently, data from separate runs of the sulphur-cycle model embedded in HadAM3 were used to parametrize the indirect effect on cloud albedo for subsequent use in the climate change experiments, as detailed in section 5 and Appendix A. Note that the effect of sulphate aerosols on cloud precipitation efficiency, the so-called 'second indirect' or 'lifetime' effect [*Albrecht,* 1989] is not modelled in this study.

3 Control simulation

The coupled model is initialized directly from the Levitus observed ocean state [*Levitus and Boyer,* 1994; *Levitus et al.,* 1995] at rest, with a suitable atmospheric and sea ice state. There is

no spinup with surface or interior ocean relaxation - the model runs freely from the start. A long control integration with fixed forcing representing late 19th century conditions was performed providing initial conditions for the climate change simulations. This run has recently been extended to over 1000 years.

The global-mean annual surface air temperature (Figure 1) shows only a very small trend of -0.010 K/century over the first 1000 years, smaller in magnitude than in the previous HadCM2 model [*Johns et al.,* 1997], despite HadCM3 not using flux adjustments or any initial spinup procedure. A slight, almost linear, drift of atmospheric mass also occurs, amounting to a reduction in mean surface pressure of about -0.244 hPa/century over the first 1000 years.

Mean climatology and variability

Gordon et al. [2000] describe some of the main features of the first 400 years of the control simulation, concentrating on the global heat budget, ocean and sea ice climatology. Although some temporal drift is apparent in the deeper ocean in its water masses and circulation, the ocean surface climatology is highly stable and generally well simulated, making the model suitable for the long climate change experiments reported here.

Seasonal mean atmospheric circulation patterns can be judged from Figure 2, which may also be compared with HadCM2 (Figure 10 of *Johns et al.,* 1997). Overall the simulation is good; probably an improvement over HadCM2 in the Southern hemisphere thanks to higher pressure in the subtropical anticyclones and reduced depth of the Antarctic circumpolar trough. In the Northern hemisphere, HadCM3's main error is that the Icelandic low is too shallow and the gradient too slack in the storm track region in DJF, an error similar to but somewhat worse than HadCM2. The North Pacific stormtrack perhaps extends too far to the east compared to the analyses. Pressure is considerably too high in JJA and particularly DJF over the Arctic, with correspondingly rather low pressure over Asia in DJF. The Asian monsoon trough is well captured in the model, however, as are the subtropical ocean high pressure systems.

In general, the model does a good job of capturing the patterns of mean seasonal precipitation for DJF and JJA when judged against the CMAP climatology [*Xie and Arkin,* 1997], illustrated in Figures 3 and 4. At most latitudes modelled zonal mean global precipitation corresponds closely with CMAP in both seasons. The agreement over land (Figure 3c,d), where the climatology is more reliable, is particularly good, giving confidence in the model physics. The split zonal-mean maximum in the tropics in DJF and strong peak in JJA are reproduced quite well (Figure 3a,b), though in JJA the model tends to shift the peak precipitation slightly equatorwards and there is rather a split ITCZ response over the W. Pacific ocean (Figures 3f;

4b). While the modelled zonal mean precipitation over the Southern Ocean appears rather high (Figure 3e,f), the CMAP reconstruction here is subject to larger uncertainty; the agreement is better in southern summer when observations are more abundant.

More detailed examination of the precipitation distribution (Figure 4) supports the view that the model is generally realistic, but some deficiencies are apparent. In both seasons the model tends to overdo the precipitation in the eastern tropical Atlantic/Gulf of Guinea, probably because local warm SST errors [*Gordon et al.,* 2000] enhance convection. In JJA particularly this tends to broaden the ITCZ too much here. Related to this, the model is rather deficient in precipitation in JJA over tropical South America.

Detailed consideration of the realism of modes of variability in the model is outside the scope of this paper, but *Collins et al.* [2000] show that ENSO-like tropical variability exhibited by the model is reasonably realistic in structure and amplitude, with better teleconnection patterns than in the previous model, and that the HadCM3 control run's modes of extra-tropical variability can be equated quite closely with the behaviour of observed North Atlantic/Arctic oscillations.

4 Anthropogenically forced experiments

The following experiments including time-varying anthropogenic forcings have been performed with HadCM3:

- G92 - forcing from observed rises in well-mixed GHGs (WMGHGs) only from 1859 to present day, thereafter the IS92a scenario for WMGHGs up to 2100.
- A92 - forcing from rises in WMGHGs as in G92, plus estimates of past changes in tropospheric ozone concentration and sulphur emissions, extended from 1990 to 2100 according to an adapted scenario loosely based on IS92a emissions.
- GB2 - As G92, with forcing due to WMGHGs only but using the B2 scenario after 1990 instead of IS92a.
- B2, A2, A1FI - forcing changes from observed rises in WMGHGs to present as G92 plus estimates of past changes in tropospheric and stratospheric ozone concentration and sulphur emissions, extended from 1990 to 2100 according to SRES B2, A2 and A1FI scenarios with estimated/modelled stratospheric ozone recovery.

G92 was initialised from year 100 of the control run and A1FI from year 470, while the remaining experiments were initialised from year 370.

Results from the A92 experiment can be obtained from the IPCC Data Distribution Centre website at http://ipcc-ddc.cru.uea.ac.uk/, but as the scenario is not standard it is not discussed

further in this paper. We concentrate here just on the other five experiments: G92, GB2, B2, A2 and A1FI.

5 Emissions, concentrations and radiative forcings

Well-mixed greenhouse gases

Concentration data for well-mixed greenhouse gases are input separately to the model for the three principal gases CO_2, CH_4 and N_2O, and also for a subset of the halocarbon species estimated to be the next largest contributors to anthropogenic radiative forcing in the recent past and next 100 years. These were CFCl3 ("CFC-11"), CF2Cl2 ("CFC-12"), CF2ClCFCl2 ("CFC-113"), CHF2Cl ("HCFC-22"), CF3CFH2 ("HFC-134a") and C2HF5 ("HFC-125"). They were assumed to have zero concentration until 1950, 1950, 1980, 1970, 1990 and 1990 respectively, with histories before 1990 taken from Table 2.5 of [*Shine et al.,* 1990].

For the historical period, CO_2, CH_4 and N_2O were as specified in the IPCC 1995 report [*Schimel,* 1996] (and *T. Wigley, pers. comm.*) based on calculations with the Bern model [*Joos et al.,* 1996].

For the future scenario part of the experiments CH_4, HFCs and HCFC-22 concentrations were calculated for the A2 and B2 cases from a continuous run of an updated version of a 2-D chemistry transport model ("TROPOS") used by *Hough* [1991]. This model runs with fixed transport, and climatologies for temperature and humidity. It was driven using SRES A2 and B2 scenario emissions [*Nakicenovic et al.,* 2000] together with estimates of natural emissions for methane from IPCC 1995 [*Schimel,* 1996], while CO_2 and N_2O data were supplied from sources working in the SRES scenario development process (M. Prather, personal communication). We adjusted output GHG values slightly near 2000 to match observational estimates and avoid discontinuity with the historical part of the scenario. In the G92 experiment, concentration values for GHGs after 1990 were instead taken directly from IPCC 1995 (Tables 2.5d and 2.5e of *Schimel,* 1996).

The GHG concentration data used to drive the A2, B2/GB2 and A1FI scenario experiments are summarized in Tables 1a-1c. G92 differs from these only slightly up to 1990.

The total GHG forcing at 2000 relative to pre-industrial is about 2.27 W/m^2 in the B2 experiment (and similar in others), towards the lower end of the IPCC estimated range (Table 2). Of this, 65% comes from CO_2 and 35% from 'minor' gases, CFCs and other halocarbons accounting for about 12%. In the future, the fractional contribution of minor GHGs falls significantly to 22% and 21% in A2 and B2 respectively by 2100, the halocarbon proportion dropping to just 4% and 5% of the total GHG forcing relative to pre-industrial (7.42 and 5.28 W/m^2) at that

time, although the absolute forcing from halocarbons shows little change.

Tropospheric and stratospheric ozone

Tropospheric and stratospheric ozone trends are calculated separately as zonal averages on the model levels, trends from one epoch to another being linearly extrapolated and added to a baseline climatology following *Li and Shine* [1995] but with a number of alterations. The more significant alterations are intended to represent "pre-industrial" conditions (the 1960s and early 1970s, not 1765 as conventional for other gases) by filling in the Antarctic ozone hole and elsewhere applying smaller changes based on SAGE ("Stratospheric Aerosol and Gas Experiment") data [*Wang et al.,* 1996]. Tropospheric ozone concentrations were calculated using runs of the three-dimensional global chemical transport model STOCHEM [*Collins et al.,* 1997; *Collins et al.,* 1999] to derive interpolated trends over the experimental period, as described in Appendix B. Climate change can affect ozone predictions [*Johnson et al.,* 1999; *Stevenson et al.,* 2000]. For the A2 and B2 scenarios only, this is allowed for approximately by using future climates, derived from the HadCM3 G92 run, in STOCHEM. This is not the case for A1FI, the 1989–90 (i.e. present day) climate from the B2 run being used instead, in order to make the forcing in A1FI more similar to corresponding experiments being conducted by other modelling groups. Further details of natural emissions etc. are described in *Stevenson et al.* [2000].

To evaluate the implied forcing from imposed ozone changes presents some difficulties in that the radiative forcing concept relates to the flux change at the tropopause, but ozone depletion at and above this level causes potentially strong adjustments in stratospheric temperatures and therefore the downward LW flux at the tropopause. The adjustment of the stratosphere to an instantaneous change of ozone would take place on a timescale of a few months and one should let these adjustments reach equilibrium before evaluating the implied forcing on the troposphere and climate system below. In this study, we therefore calculate the forcing by first calculating the stratospheric radiative heating/cooling rates using the control run (unperturbed forcing), assuming the stratosphere to be in radiative and dynamical balance. We assume that under imposed ozone changes the dynamical changes are negligible. Hence to maintain equilibrium, radiative heating rates must also remain unchanged. To achieve this, iterative calculations are performed off-line from the model experiments themselves, in which stratospheric temperatures are adjusted under the imposed ozone changes until the radiative heating rates return to the reference values. This method is referred to as the 'fixed dynamical heating' (FDH) approximation (eg. *Ramanathan and Dickinson,* 1979). Ozone distributions for selected years of the coupled model experiments are iterated using this method for monthly mean states from a two

year section of the control run and the radiative flux changes at the tropopause averaged over the two years to derive the approximated radiative forcing in the experiments.

The FDH approximation could be unrealistic if significant dynamical adjustments also occur in the stratosphere in response just to ozone changes. We can judge this to some extent by examining the radiative and dynamical balance in the forced experiments themselves (see section 6), although other forcings and feedbacks may amplify or reduce these dynamical changes. An alternative method of calculating the ozone forcing interactively [*Tett et al.,* 2001] yields a significantly higher estimate of the effect of stratospheric ozone changes than the FDH method, for reasons that are not yet fully understood.

Sulphur and sulphate aerosols

As mentioned in Section 2, the direct radiative effect of sulphate aerosols is determined explicitly from the anthropogenic burdens and physical state of the atmosphere.

To determine the indirect sulphate forcing effect, a more complex calibration procedure was required as described in Appendix A. The anthropogenic forcing changes were applied in the HadCM3 experiments via specified cloud albedo perturbations based on prior calibration experiments performed off-line using HadAM3, which had the natural and anthropogenic emissions included with present-day climate. This method avoids the need to include the natural sulphur cycle explicitly in the control and forced HadCM3 experiments, which would have been more expensive computationally. The technique produces an indirect aerosol forcing distribution in HadCM3 similar to that in the HadAM3 calibration runs but typically of about 70% of the magnitude, the discrepancy arising from at least three sources:-

- Limitations of the parametrized method; eg. running into limits on the cloud effective radius, and so being unable to produce the desired amount of forcing, and the fact that the simple measure of cloud albedo used may not accurately track the (complex) changes in cloud radiative properties which actually produce the forcing.

- Problems with time-averaging such that the forcing associated with timestep-by-timestep changes in cloud albedo (as in the HadAM3 calibration runs) is not the same as that produced by an annual-mean of these albedo changes (as used in the HadCM3 experiments).

- Differences in the meteorology in the simulations, particularly in the distribution of clouds which will produce differences in the forcing locally.

Given the large uncertainty in estimates of the indirect effect (eg. *Schimel,* 1996), this imperfect method was nevertheless considered good enough for this study.

The variations in sulphate aerosol burdens and forcings in A2, B2 and A1FI are illustrated in Figure 5, with linear interpolation between the calibration years which are marked with symbols. One year re-runs were performed with additional radiation computations to derive these forcings.

In accordance with the emissions scenarios, the global-mean burden and forcing both rise sharply in A2 and A1FI, peaking at 2030 (between the 2000 and 2050 data points plotted in Figure 5) before falling back at 2100. (A regional breakdown of the anthropogenic emissions in the A2, B2 and A1FI scenarios is given in Table 1d). The global burden in B2 (Figure 5a) remains quite level over the 21st century despite a marked decrease in emissions from 69.0 to 47.3 Tg[S]/year between 2000 and 2100, and in A2 the burden at 2100 is considerably higher than 2000 despite the reduced emissions (60.3 Tg[S]/year at 2100).

A pronounced rise in the sulphate burden/emissions ratio is thus apparent through the simulations (Figure 5c). The most significant factor is the migration through time of emissions to subtropical and tropical regions where oxidant concentrations are much greater than in mid-latitudes and therefore more efficient for sulphate production - the rise is a consequence primarily of the geographical characteristics of the emissions scenario, therefore. There is also a slow accumulation of sulphate in the stratosphere in the model, but separate HadAM3 experiments with present-day SSTs and GHG concentrations have shown that this is only a minor contributory factor. It should be noted here that variations of oxidant concentrations in response to climate change would be expected to modulate the burden/emissions ratio as well, but we do not model this effect.

In B2 the direct forcing remains fairly constant between 2000 and 2100 (Figure 5b) like the burden, but the indirect forcing reduces significantly. To a good approximation the direct forcing scales linearly with the global sulphate burden, but this is clearly not the case for the indirect effect. The normalized indirect forcing (i.e. forcing per unit sulphate burden; Figure 5d) weakens by a large factor (more than a factor of 4 between 1860 and 2100 in B2) as the sulphate burden increases. This is expected partly because the radiative sensitivity to adding further sulphate at a given location decreases with increasing aerosol. In our formulation of the effect, given that any points where the albedo perturbation would give rise to a cloud albedo greater than unity have their albedos limited, one would also expect this to compound the drop-off of the normalized indirect forcing at high aerosol concentrations, eg. at 2050 in A2. The difference in normalized indirect forcing between 2000 and 2050/2100 in B2 (despite similar global sulphate burdens) is probably mainly due to the main areas of pollution moving to lower latitudes where cloud is both less abundant and less susceptible to this indirect effect.

It may seem a little surprising at first sight that the fossil-fuel-intensive scenario A1FI gives rise to a lower sulphate burden at 2050 than A2, with consequently weaker aerosol forcing.

Indeed, at 2100 the A1FI aerosol burden is lower even than in the B2 case. However, A1FI is an amalgamation of the A1C and A1G scenarios [*Nakicenovic et al.,* 2000]. Of these, A1C assumes heavy use of coal, but burned using 'clean' technologies that reduce sulphur emissions; while A1G assumes heavy use of oil and gas, fuels which contain less sulphur.

Net radiative forcing

The rate of increase in net radiative forcing in the B2 scenario is similar to that over recent decades (Figure 6), and reaches about 4.5 W/m^2 by 2100. In other words, this scenario continues the recent trend. If only well-mixed GHGs are considered (as in GB2), the net radiative forcing in is about 1 W/m^2 higher in 1990, but converges towards that in B2 by the end of the 21st century (Figure 6). This follows from the gradual decrease in sulphur emissions and consequent weakening of that forcing in B2 in the second half of the century (Table C1, Figure 5b).

The forcings in A2 and A1FI diverge sharply from B2 in the 2040s and 2020s respectively (Figure 6), following the rapid increase in the rate of CO_2 and other GHG emissions relative to B2 at those times (Table 1). Initially, the forcing increases much faster in A1FI because GHG emissions increase faster, and sulphur emissions are lower. Towards the end of the 21st century, however, this trend is reversed - sulphur and CO_2 emissions rates are then similar in both scenarios, but the emission rates of some trace gases (eg. CH_4, HFC-134a) become much higher in A2 (inferred from Table 1). By 2100, the net heating is 6.7 and 7.4 W/m^2 in A2 and A1FI respectively, compared to just over 6 W/m^2 in the old G92 scenario.

6 Climate change response

Global warming, sea level, and sea ice trends

Of the five scenario experiments G92, GB2, A1FI, A2 and B2 the first two (GHGs only) exhibit overall global warming from 1900 to present somewhat above the observed, whereas the latter three (including other anthropogenic forcings) agree much better with the observed change, represented here by an updated version of the blended MOHSST6-UEA SST and surface air temperature dataset [*Parker et al.,* 1994] (Figure 7a). Note however that the rate of global warming in recent decades is similar in all cases (A1FI, A2 and B2 being identically forced up to 1989). It is plausible that the inclusion of all anthropogenic forcings in the A1FI, A2 and B2 cases is more realistic in representing the 20th century record, but it is not the purpose of this paper to deal with detailed attribution analyses. For the sake of discussion of the future forced responses we simply assume that the results are a reasonable guide to the future given the scenario inputs, but a number of caveats are also discussed later.

Relative to 1900, predicted global warming spans a range of about 1.5 to 2.5 K at 2050 rising to 2.9 to 5.2 K in 2100. The upper envelope is defined by G92 and GB2 up to about 2050, but A1FI warms most thereafter, while the lower envelope is provided by A2 up to about 2030 and thereafter by B2. The A2 and A1FI warmings rise particularly steeply in the mid 21st century, following the increase of emissions discussed in Section 5. Over the last decade or so of the 21st century A1FI is warmer than the other scenarios by a clear 1 K or more (Figure 7a). The global mean temperature response essentially tracks the graph of estimated global mean forcing through time in the four experiments (Figure 6), with a warming at 2100 of about 0.55-0.65 K/$[W/m^2]$.

Land and sea temperatures (Figure 7b) mirror the rise in global means but with a fairly consistent land-sea contrast in the transient response with a land/sea ratio of about 1.7; higher than in some other models (eg. ECHAM4-OPYC; *Roeckner et al.,* 1999 - hereinafter referred to as R99), but similar to that in HadCM2 [*Mitchell et al.,* 1999].

Sea level rise is an important consequence of climate change, leading to both the relatively slow inundation of low-lying coastal areas and an increase in the frequency of short lived extreme high water events. The largest contribution to the predicted rise in future global-mean sea level during the period 1900 to 2100 is from the thermal expansion of the ocean, calculated from the changes in temperature structure of the model ocean [*Gregory and Lowe,* 2000]. Relative to 1900, the predicted thermal expansion ranges from 22 to 33 cm (Figure 8), largest for A1FI. The rate of sea level rise is particularly steep for A1FI and A2 after 2050. When a (provisional) estimate of the contribution to sea level rise from the melting of land ice is also included [*Gregory and Lowe,* 2000], the total increase in mean sea level ranges from 32 cm to 48 cm. Because of the long timescales associated with sea level rise, even if the concentrations of atmospheric CO_2 were stabilised at 2100, the sea level would continue to rise for at least several centuries.

While sea level is predicted to rise almost everywhere, there is considerable spatial variation. In some regions, the rise is slightly negative or close to zero, in others up to twice the global mean. The predicted patterns of sea level rise (not shown) exhibit the largest increases in parts of the north Pacific and to the west of Greenland. For A2 (the central member of the 5 scenarios considered here), the maximum rise is 75 cm, occurring in the northwestern Pacific, near Japan. However, *Gregory et al.* [2001] recently compared the patterns of sea level rise predicted by different climate models for the same emissions scenario and found many of the regional details to be model-specific. Thus, our confidence in the predicted spatial patterns of sea level rise is currently less than for temperature change patterns.

Melting of sea ice in response to global warming becomes apparent in the second half of the 20th century (Figure 9), at least in G92 and GB2 which produce quite marked thinning of

Arctic ice. The decline in Arctic ice in B2 over this period is less pronounced, though it starts to accelerate late in the century. Both area and volume of Arctic ice continue to decline strongly in all five cases throughout the 21st century, the relatively more rapid decrease in volume indicating that the remaining ice continues to thin. By 2100 the annual mean areal coverage in the Arctic falls to between about 40% (A1FI), 50% (A2,G92) and 60% (B2, GB2) of that in CTL, and the annual mean volume to between about 25% and 40%. A similar but smaller decrease also occurs in Antarctic sea ice (not shown), with much less variation between the five experiments. In 2100 there is a decrease in area and volume to about 60% and 50% respectively of that in CTL.

Trends in the hydrological cycle and energy balance

Global-mean annual precipitation (not shown) is enhanced in the warmer climate, with a sensitivity around 1%/K (about 1.4%/K in the GHG-only scenarios). The cloud feedbacks are almost neutral, at least in the GHG-only cases G92 and GB2, as shown by the change in net cloud forcing (Table 3). (This diagnostic cannot be used to determine the cloud feedback in the A1FI, A2 and B2 experiments as it is affected by an increase in upward solar flux and small decrease in LW flux due to the sulphate aerosols). There is enhanced radiative cooling of the atmosphere in all the experiments (balanced mainly by increased latent heat of condensation) (Table 3) and increased radiative heating of the surface (mainly due to reduced longwave cooling) which is balanced by increased evaporation (Table 3). Over the sea, increased radiative heating at the surface is balanced mainly by enhanced evaporative cooling, whereas over land, the balance is maintained through enhanced sensible heat (Table 3). This arises because evaporation is restricted over parts of the continents, and the surface temperature is generally higher over the ocean than over well-watered land, making evaporation a more efficient means of losing energy than sensible heat. There is an increase in the flux of moisture from ocean to land in all experiments.

The global sensitivity of precipitation for a given warming is much higher than in ECHAM4-OPYC (R99). The reasons for the difference are not clear, especially as only the G92 and R99 GHG experiments are directly comparable. On examining the changes in these two experiments for the 2040s when the global mean warmings in G92 and GHG are 2.43 K and 2.39 K respectively (Table 4), one finds that the increases in the net downward flux at the top of the atmosphere is similar in both experiments, but that there is a greater increase in the radiative heating of the surface in G92 3.7 W/m^2 cf. 2.2 W/m^2, and less in the atmosphere: -3.0 W/m^2 cf. -0.77 W/m^2 (Table 4). Thus, in G92 the surface is being warmed and atmosphere cooled relative to GHG.

This is balanced by greater surface evaporation and atmospheric condensation (precipitation) in G92.

The shortwave cloud feedback is negative in GHG (R99) but weakly positive in G92 (the resultant of a positive feedback over land and negative feedback over sea; Tables 3a-c). This will contribute to the smaller increase in surface heating in GHG. *Boer* [1993] argued that the rate of increase in precipitation in their model/K warming was less than in most other models because of a negative shortwave cloud feedback. The differences in the changes in radiative cooling of the atmosphere are most likely due to differences in the changes in longwave radiation, though this cannot be inferred directly from the available diagnostics. A smaller increase in longwave cooling of the atmosphere in GHG would be consistent with a smaller increase in precipitation. The main difference in precipitation changes is over the ocean where precipitation increases by 1.7%/K in G92 over by the 2040s, whereas it decreases in GHG.

Signal to noise ratio is well known to be lower in the precipitation response than for temperature changes. This is most markedly illustrated in the contrast between land and sea precipitation responses (Figure 10). While a consistent trend signal is clear for sea points, the trends in global-mean land precipitation are extremely variable even after smoothing to filter sub-decadal timescales. Only G92 shows anything resembling a consistent rising trend for global-mean land precipitation; GB2 shows an initial rising trend similar to G92 up to 2050 but then a fall back to near the control run value at 2100. Of note is the fact that A1FI, A2 and B2 show falling trends up to present day by contrast with G92 and GB2, since this might provide some discrimination in detection and attribution studies. Future trend projections in A1FI, A2 and B2 are variable, with little overall change from CTL by 2100. Interdecadal variability in A2 in the future appears higher than in B2 but the reasons are not examined further in this paper.

In most of the following analysis we concentrate on 30-year averages, of annual and seasonal mean (DJF and JJA) variables in order to enhance the signal-to-noise ratio. Two future periods, the '2040s' (the 30-year period from Dec 2029 to Nov 2059) and the '2080s' (similar but 2069 to 2099) are analysed. Differences are constructed relative either to a 240-year period of CTL parallel to the forced experiments, or relative to a 30-year present-day period, the '1980s' (as before but 1969 to 1999). In order to estimate noise we use the standard deviation of successive 30-year averages from CTL (see *Collins et al.* [2000] for more detail on the variability in CTL), and estimate significance levels assuming 30-year average signals sampled from the forced experiments are Normally distributed about a mean signal level with standard deviation as estimated from CTL, i.e. with no change of variance in response to forced climate changes.

Geographical annual-mean and seasonal signals

Although global-mean changes are useful as a summary of the responses to the different emissions scenarios, the geographical distribution of the changes is needed to determine the impact of the different scenarios. Here we list the main features of the geographical patterns of response in temperature, precipitation and soil moisture. The changes are formed by subtracting a long term mean from the control simulation from the '2040s' or '2080s' mean for each scenario. We also note the main effects of including aerosols in the B2 scenario, and the key differences from the patterns obtained using an earlier model, HadCM2 (*Mitchell and Johns,* 1997 - hereinafter referred to as MJ97). We have not tested the statistical significance of the patterns of change, but as it turns out, the large scale features are remarkably consistent for the three scenarios considered. In the next subsections, we consider specific regions and assess statistically the changes in selected parameters.

Annual mean temperature

The patterns of temperature change are similar in the three scenarios B2, A2 and A1FI (Figure 11), with a warming everywhere that gets progressively larger in going from B2 to A2 to A1FI. The patterns are similar to those obtained in other models (eg. *Kattenberg et al.,* 1996) - the warming is larger over land than sea, and largest in and around the Arctic. The warming is less than the global average over the northern North Atlantic, much of the Southern Ocean and over Southeast Asia. There is a large warming over the Amazon basin which is not always found in other models.

The effect of sulphate aerosols in the B2 scenario is to reduce the warming, especially in the northern hemisphere (Figure 11d). In fact much of the northern continents around 45°N are 1 K or more cooler than in the case with GHGs only.

There is less warming in the tropics and more in the extra-tropics than in experiments using HadCM2 – see MJ97. In HadCM2, there was a secondary maximum in the warming in the tropics which arose from differences in the treatment of cloud and the boundary layer – see *Williams et al.* [2001a] for a detailed analysis of the differences in the response of the two models.

Precipitation

As with temperature, the patterns of change in precipitation are similar, with the smallest changes in B2 and the largest in A1FI (Figures 12, 13). There are increases in the extratropics associated with enhanced poleward transport of moisture arising from the increase in

atmospheric humidity (eg. [*Manabe and Wetherald,* 1975]) and decreases over much of the subtropics. Precipitation generally increases along the Intertropical Convergence Zone (ITCZ) although there are also some regions of decrease. Over the tropical oceans, there are increases to the north of the equator and decreases to the south. This is symptomatic of a northern shift in the ITCZ associated with the warming being greater in the Northern Hemisphere, and hence displacing the "thermal equator" northwards. A similar northward shift was noted in an earlier experiment [*Murphy and Mitchell,* 1995].

In northern summer, the area of decreases in the subtropics extend further north into the United States, Europe and much of central Asia (Figure 13). In general, summer monsoon precipitation increases (over Southeast Asia and parts of Africa during June to August, and eastern South America, East Africa and Northeast Australia during December to February). The main exception is the northern part of the Amazon Basin, where precipitation decreases throughout the year. The increases in precipitation in high southern latitudes are more pronounced and extend further north during June to August then December to February.

Adding aerosol effects in the B2 scenario has only a small effect on precipitation, generally weakening the response (Figure 12d, 13d). Note particularly the reduced increases over Southeast Asia and smaller reductions over southern Europe during June to August (Figure 13d). This is similar to the response to aerosols noted by MJ97 using an earlier model in which the effect of aerosols was represented by an increase in surface albedo.

By contrast with MJ97, the precipitation increases are shifts to the north rather than an in situ enhancement. This is consistent with the differences in the change in zonally averaged temperatures - in HadCM3, there is greater warming in the Northern Hemisphere leading to a northward shift in the ITCZ; in MJ97, there is local maximum in the warming at the equator which enhances the ITCZ where it is. A more detailed analysis of the reasons for the difference in response of the two models is given by *Williams et al.* [2001a]. A second major difference is that there are decreases in precipitation during June to August over much of the northern mid-latitude land surface including the United States and Europe, and increases over India (Figure 13), whereas MJ97 found little change or increases in mid-latitudes, and a drying over much of India at this time of year. Climate impact studies using the two sets of results are likely to come to very different conclusions.

Soil moisture

Once again, the patterns of change are very similar in the A2, B2 and A1FI scenarios. In the Northern Hemisphere, the changes are much as one would expect from the changes in

precipitation - the northern extratropical continents are wetter in winter (Figure 14), but become drier than in the control climate over much of North America and Europe in summer (Figure 15). Northern Canada and Siberia are wetter all year, as are regions affected by tropical monsoons, except for the northern part of South America. The changes over Australia vary from scenario to scenario.

The main differences from MJ97 are evident during June to July, when the tropics and subtropics are wetter rather than drier, and Europe is drier rather than wetter. These differences arise partly from the different patterns of temperature response, and partly from the changes made to the land-surface parametrizations (see *Williams et al.,* 2001a).

Regional signals and their significance

The climate change response of annual-mean temperature, DJF and JJA precipitation in the 2040s and 2080s relative to the 1980s is summarised in Tables 5a-5c for the globe and five selected land regions defined and assessed previously by IPCC [*Houghton et al.,* 1990; *Houghton et al.,* 1996]. We do not consider the fidelity of the control simulation, just the signals of climate change and their significance for these regions.

Not surprisingly, all five scenario experiments give significant warming in annual-mean temperatures over all regions, the highest warming being in the mid-USA (reaching +4.88 K in A2 and +6.61 K in A1FI in the 2080s), and the lowest in Australia (just +2.05 K in B2 in the 2080s). S. Europe and the Sahel warm slightly less than the mid-USA, but more than S. Asia and Australia to maintain a generally north-south gradient in land temperature response, except that the Sahel warms relatively strongly compared to S. Europe (particularly in the GHG-only experiments in the 2080s).

Comparison of the response in B2 minus GB2 (i.e. the effect of additional anthropogenic forcings in the B2 scenario) reveals only small differences for these land regions - S.Asia is significantly colder in the 2040s, and Australia colder in the 2080s in B2 relative to GB2; all other differences are insignificant. Globally, B2 is colder than GB2 in the 2040s, but recovers to match GB2 by the 2080s as a consequence largely of the small net change in sulphate forcing between the 1980s and 2080s (Figure 5b).

Seasonal DJF and JJA precipitation responses (Tables 5b,5c) in the five scenarios are not significant in some cases, but globally there is a significant increase in all scenarios (tending to be higher in the GHG-only cases). A1FI has the largest global precipitation increase overall in the 2080s, consistent with its strongest global warming signal. The mid-USA shows an increasing trend towards wetter winters (particularly in A1FI and A2 in the 2080s) but a marked trend

towards drier summers (significant in all five scenarios for both periods). S. Europe generally shows no significant change in winter precipitation apart from a significant increase in B2 by the 2080s, while in summer there is a significant drying in all five scenarios in both periods. In the Sahel, there is essentially no change in DJF precipitation at all in any scenario (the bulk of the region staying extremely dry throughout), but a more complex response in JJA with an initial tendency towards wetter summers in the 2040s, most marked in G92 and B2, subsequently reduced or reversed back to little significant change by the 2080s. S. Asia is the only region with clear and consistent signals in both seasons, namely drier in DJF and wetter in JJA in all cases. The increase of 1.76 mm/day in JJA in the 2080s in A1FI is particularly noteworthy. Australia has a relatively large standard deviation in DJF precipitation in the control which makes most of the tabulated changes non-significant, but the consistent sign (apart from the 2040s in A1FI) suggests that somewhat drier conditions are likely here in future; while in JJA no significant changes are expected in four of the five scenarios, the exception being A1FI which is significantly drier in the 2080s. In Australia, however, the regional average may obscure some significant local detail in that the monsoon response affects certain parts of the continent differently from others.

Overall, regional annual temperature and seasonal precipitation changes over the next 100 years relative to present day indicate that under the B2 scenario little difference can be expected on adding anthropogenic factors other than GHGs, due to the relatively flat sulphate forcing for this scenario. This observation would presumably not apply in other scenarios that have stronger trends in sulphate forcing over this period. By contrast, significant differences between A2 and B2 are predicted for mid-USA and S. Europe (both tending to larger summer drying in A2 than B2), and S. Asia (tending to enhanced summer monsoon, stronger in A2). It is also worth noting that for the Sahel region the initial trend towards enhanced JJA precipitation in the 2040s may be reversed by the 2080s, leading to the possibility of higher water stress. In other regions the trends in 2040s tend to be amplified in the 2080s. As expected, the highest overall emissions scenario A1FI produces the most dramatic local warmings by the 2080s, particularly for the mid-USA region, and notably large precipitation increases in S. Asia in JJA, undoubtedly with implications for heightened risk of flooding.

7 Conclusions and future work

The simulations described in this note incorporate a number of novel features. They use a set of emission scenarios derived from a self-consistent set of social and economic assumptions. They include changes in all the main greenhouse gases explicitly, some experiments including ozone trends derived using separate comprehensive models of atmospheric chemistry. Sulphate aerosol burdens have been calculated interactively in the climate model, and both the direct scattering effect of sulphate aerosols and their indirect effect on the reflectivity of water clouds have been included. The climate model includes several advances, including relatively high resolution in the ocean, allowing the model to be run without artificial flux adjustments, and improvements to the representation of the land surface.

In the B2 scenario, CO_2 emissions are lower than under IS92a, whereas in A2 and A1FI, GHG emissions eventually increase faster than in IS92a. In B2 sulphur emissions decrease throughout the 21st century, whereas in A1FI, and especially A2, they increase but then decrease. In all three scenarios, the global-mean forcing due to aerosols is weaker in 2100 than in 2000, although the distribution also changes. The response to the five scenarios considered differs little over the next two decades, with a rate of global-mean warming similar to that seen in recent decades. However, by the middle of the 21st century, the global-mean warming in A2 and A1FI is noticeably greater than in B2, and by the end of the century, is greater than in IS92a (without aerosols).

Global-mean sea level rise between 1900 and 2100 is predicted to be in the range 32 to 48 cm, with the upper value corresponding to the A1FI scenario. The largest contribution to sea level rise is from thermal expansion.

There are several pronounced differences in the modelled regional changes compared to an earlier study (MJ97): the secondary maximum of warming in the tropics is no longer present, there is a general northward shift in tropical precipitation as opposed to an in situ enhancement, and much of the northern mid-latitude continental land mass becomes drier in summer, as opposed to becoming wetter or changing little.

Analysis of regional climate change signals confirms a wide variation in annual mean warming between five land regions and across scenarios. The mid-USA has the largest warming, in the 2080s reaching 6.6 K relative to present in the A1FI scenario. There is a clear tendency for drier DJF and wetter JJA seasons in S. Asia through the 21st century, most pronounced in the A1FI scenario. In JJA, S. Europe and mid-USA become increasingly dry in all scenarios. For the Sahel and Australia precipitation changes are less significant compared to modelled natural variability, but there are nonetheless general trends towards wetter conditions in the Sahel mid-

century, and some overall drying in Australia at the end of the century. In DJF, mid-USA and S. Europe regions eventually tend to become slightly wetter while Australia becomes drier.

There are several ways in which this work could be extended or improved:

- First, extra SRES scenarios could be considered. The B1 scenario is already being run, and the results will be described in an updated version of this note. This leaves the A1 scenario as the only one of the four marker scenarios that we have not considered.

- Second, it seems likely that the sulphur burdens produced in the sulphur cycle model are too low. Improved versions of the sulphur cycle now exist, and could be used in future experiments. However, a bias towards low sulphur burdens may not imply a bias towards an indirect albedo forcing that is too small, as any low bias due to underestimating the anthropogenic increase in sulphate burden will be compensated to some extent by an overestimate of the susceptibility of clouds to the indirect effect. The latter arises because the natural level of aerosol burden is also underestimated, and the indirect effect depends non-linearly on this base level.

- Third, there are considerable uncertainties in modelling the indirect effect of sulphate aerosol. The "first" indirect effect is represented here approximately and non-interactively, and the "second" indirect effect omitted. Both have been included interactively in a revised version of an atmospheric model coupled to a simple ocean [*Williams et al.,* 2001b], but have not yet been incorporated in a fully coupled model. The second indirect effect (increasing cloud lifetimes) is likely to lead to an additional negative forcing.

- Finally, there are a number of feedbacks and factors which have been ignored. We have not included the effect of climate change, principally the increase in water vapour, on future methane concentrations [*Stevenson et al.,* 2000]. We have omitted the effects of changes in soot, mineral dust and biogenic aerosols. Soot is likely to give an additional warming whereas biogenic aerosols are likely to cool, but even the sign of the global mean dust forcing is not certain. Although estimates of the current level of these effects exist, they are not well known and the SRES scenarios do not provide estimates of future emissions of these substances. We have also neglected land surface changes and natural forcings (solar variations and volcanoes).

Appendix A. Calibration of indirect sulphate aerosol forcing

Annual-mean distributions of sulphate aerosol were generated from HadAM3 model runs which include the sulphur cycle. Only natural emissions were used for the pre-industrial era, namely

emissions of DMS [*Kettle et al.,* 1999; *Liss and Merlivat,* 1986] and volcanic emissions [*Andres and Kasgnoc,* 1998]. Anthropogenic emission scenarios were added to the natural emissions for the years 1860, 1900, 1950, 1975, 2000, 2050 and 2100 (see Appendix C). Successive pairs of these sulphate distributions (e.g. pre-industrial and 1860; 1860 and 1900) were then used as input to 1-year runs of HadAM3 with climatological (present-day) sea surface temperatures and sea ice. The version of HadAM3 used was identical to the atmospheric component of HadCM3 except that it used the relation of *Jones et al.,* 1994 to predict cloud droplet number concentration (N_d) rather than the fixed N_d values used in the HadCM3 control run. Concentrations of sulphate and (over the oceans) sea-salt aerosols were used as input to this relation to determine N_d [*Jones et al.,* 1999], subject to a minimum value of 5 cm^{-3}. For each model run the shortwave radiation scheme was called twice, once with the earlier sulphate distribution and once with the later. In each case a simple measure of cloud albedo α was calculated [*Bohren,* 1980]:

$$\alpha = \tau(1-g)[2+\tau(1-g)]^{-1} \tag{1}$$

This assumes conservative scattering, and in approximating the indirect effect we also assume a fixed asymmetry parameter g (=0.85) and use the fact that the optical (extinction) cross-section of a particle much larger than the wavelength is twice its geometrical cross-section [*Bohren and Huffman,* 1980].

For each 1-year HadAM3 model run using a pair of sulphate scenarios, the distribution of the change in α caused by the changes in aerosol was stored and used to build up a history of the change in cloud albedo ($\Delta\alpha$). If $d\alpha_1$, $d\alpha_2$ etc. represent the changes in cloud albedo for the sulphate distributions pairs {pre-industrial,1860}, {1860,1900} etc. respectively, then the cloud albedo change at each "marker" year is calculated by summation:

$$\begin{aligned} \Delta\alpha(1860) &= d\alpha_1 \\ \Delta\alpha(1900) &= d\alpha_1 + d\alpha_2 \\ &etc. \end{aligned}$$

Cloud albedo changes between these dates were obtained by linear interpolation.

These cloud albedo changes were used to simulate indirect forcing in the HadCM3 runs as follows. The change in α due to the change in aerosol distribution corresponds to changing τ by a factor λ:

$$\Delta\alpha = \lambda\tau(1-g)[2+\lambda\tau(1-g)]^{-1} - \tau(1-g)[2+\tau(1-g)]^{-1} \tag{2}$$

Re-arranging (1) to give an expression for τ and then substituting into (2) yields:

$$\Delta\alpha = \lambda\alpha[(1-\alpha)+\lambda\alpha]^{-1} - \alpha \tag{3}$$

Following *Platnick and Twomey,* 1994, we define a factor χ, the fractional change of N_d corresponding to the fractional change λ in τ. As τ is inversely proportional to the cloud droplet effective radius r_e, and as r_e is proportional to $N_d^{-1/3}$ [*Martin et al.,* 1994], then we can replace λ by $\chi^{1/3}$. Re-arranging (3) then gives:

$$\chi = [\Delta\alpha(\alpha-1) - \alpha(1-\alpha)]^3[\alpha(\Delta\alpha+\alpha-1)]^{-3} \tag{4}$$

At each timestep in the HadCM3 run the fixed values of N_d and the predicted cloud water content were used to derive an initial value for r_e using the parametrization of *Martin et al.,* 1994. Cloud optical depth τ was then calculated and used to derive an initial distribution of α using (1). The distribution of $\Delta\alpha$ for the appropriate time was available from the offline history produced from the HadAM3 runs and used in conjunction with α to calculate χ using (4). Note that at this point in the model r_e has only been used to determine the initial distribution of α. Before r_e was used in the radiation code for a full calculation of cloud radiative properties it was modified to r_e' using χ to approximate the indirect albedo effect:

$$r_e' = r_e\chi^{-1/3} \tag{5}$$

It is possible for χ to be infinite, zero or negative, implying either: (i) that the decrease in cloud albedo required is greater than ($\chi < 0$) or equal to ($\chi = 0$) the current value of α, and in such cases the cloud was made as dark as possible by setting r_e to the maximum value allowed (37 μm); or (ii) that the increase in cloud albedo required to produce the desired forcing, when added to α, produces a result which is greater than ($\chi < 0$) or equal to ($\chi \to \infty$) unity, and in such cases the cloud was made as bright as possible by setting r_e to the minimum permitted value (0.35 μm). Both these factors may exert a limiting influence on the forcing actually produced in the coupled run, as may differences between the cloud distribution of the coupled run and of the atmosphere-only runs used to generate the albedo-change history. It is too computationally expensive to calculate the actual forcing experienced by the coupled model as the simulation evolves as this would require multiple calls to the (computationally intensive) radiation scheme. Consequently, 1-year portions of the simulations were re-run with extra radiation calls and diagnostics for the scenario years 1860, 1900, 1950, 1975, 2000, 2050 and 2100. The ideal forcing for these years was available from the separate HadAM3 runs used

to generate the albedo-change history, and this was compared with the actual forcing produced in HadCM3 in these years.

Appendix B. Computation of ozone trends

In the troposphere the ozone trends are constructed by means of off-line 3-D chemical transport (STOCHEM - *Collins et al.,* 1997; *Collins et al.,* 1999) model simulations for specific epochs 1990, 2030, 2060 and 2100; each simulation being run for 15 months. Intermediate results are obtained by linear interpolation in time. Initial methane concentrations are provided from an earlier run of the 2-D TROPOS model. Emissions for 1990 are based on those from the EDGAR database [*Olivier et al.,* 1996], with future emissions taken from the SRES scenario definitions themselves. The 3-D STOCHEM model runs are also meteorologically and dynamically forced with six-hourly data from a previous HadCM3 coupled experiment which to first order reflects the climate conditions (eg. global warming) expected at the appropriate time.

For the purpose of extrapolating stratospheric ozone depletion into the future, 'effective equivalent stratospheric chlorine' (EESC) contributions were estimated for Cl and Br compounds not already included in the 2-D model used for computing well-mixed minor GHGs by means of a simple box model driven using SRES and natural emissions where appropriate. Tropospheric mixing ratio estimates from this and the 2-D model for years from 1950 to 2100 were then combined and used to calculate stratospheric ozone as a function of height, longitude and month making the following assumptions:

- That it takes 3 years for tropospheric chlorine and bromine to get into the stratosphere.
- That bromine is 40 times more effective in destroying ozone than chlorine.
- That prior to 1974 there was no stratospheric ozone depletion.
- That ozone is depleted linearly by EESC (=Cl+40*Br) levels above the 1974 stratospheric level, any implied negative ozone values being replaced by zero.
- From 1974 to 1979 ozone fell at half the rate, and from 1979 to 1998 at the full rate given by the SPARC (Stratospheric Processes And their Role in Climate) trends [*Randal and Wu,* 1999]. The SPARC trend (ozone/year) was converted to ozone loss per EESC using a linear regression fit and dividing by the mean EESC trend for 1979–98.

Zero ozone change was imposed at the tropopause model level, as estimated from the 1871-1990 mean tropopause height of a HadAM3 integration forced by the observed sea surface

temperatures and sea ice extents from the GISST3.1 data set (an updated version of that described in *Rayner et al.* [1996].

Appendix C. Anthropogenic sulphur emissions.

Only anthropogenic emissions were included in the experiments. For the 'past' portion of the experiments, the basic datasets we use are the revised version of the 1985 GEIA 1B dataset (released in June 1997) and the University of Stockholm [*Orn,* 1996] historic emissions datasets for 1860, 1870,... 1970. The GEIA 1B dataset includes seasonal variations over some regions, eg. Europe, but for convenience we employ an annually averaged version. In any case the Stockholm datasets are annual means. The GEIA 1B dataset also splits the emissions into those from near-surface and elevated sources; experiments have shown that the sulphate distribution is quite sensitive to the level of emission, so we preserve this split.

For the 'future' portion of the experiments, we used two of the four preliminary versions of the possible marker scenarios (labelled A1, A2, B1 and B2) produced by the IPCC SRES group, namely A2 and B2. We also used the 'fossil fuel intensive' variant of the A1 scenario developed at a later stage, known as A1FI. Of these, A2 is perhaps the nearest to the formerly much-used IS92a 'business-as-usual' scenario as it predicts a substantial increase in global SO_2 emissions in the first 3 decades of the 21st Century, though not to as large a peak as in IS92a. The global total emissions in the A1FI scenario also rise to a peak, in 2030, but drop steeply thereafter. In contrast, the global total emissions in the B2 scenario decline gently throughout the 21st Century (see Table C.1).

The SRES SO_2 emissions are provided on a regular lat-long grid at a resolution of $1^\circ \times 1^\circ$. Fields are available at ten year intervals from 1990 to 2100. It should also be noted that the SRES group harmonised the scenarios to ensure that the emissions fields are the same for all 4 marker scenarios in both 1990 and 2000. The complete sequence of base dates, between which emissions are found by interpolation, is therefore 1860, 1870,... 1980, 1985, 1990, 1995, 2000, 2010, ... 2090, 2100. (Note that the spacing alters at 1980 and 2000). The purpose of the 5 year intervals between 1980 and 2000 is that we actually do use the GEIA 1B data at 1985 (with minor differences due to time interpolation), which should be more accurate.

We define a two-dimensional field $\mathcal{F}$ by

$$\mathcal{F}(x,y) = \frac{H(x,y,1985)}{H(x,y,1985) + S(x,y,1985)}$$

where $H(x,y,1985)$ is the GEIA 1B elevated emission field and $S(x,y,1985)$ is the GEIA 1B surface emission field. $\mathcal{F}$ is thus the fraction of the emissions from elevated sources. (Where there are no emissions in 1985 $\mathcal{F}$ is set to zero.) We use this field to split the Stockholm historic

datasets into surface and elevated components. Clearly the fraction of emissions from elevated sources has varied in time, so we introduce a factor $\phi(t)$ to describe this. We assume that $\phi(t)$ is zero before 1950, 1 after 1985 and varies linearly with time between 1950 and 1985.

The 1980 fields are constructed by interpolating the 1985 and 1970 fields linearly, *e.g.*

$$H(x, y, 1980) = \frac{2H(x, y, 1985) + H(x, y, 1970)}{3},$$

and similarly for S.

We have no information about possible changes in $\mathcal{F}$ in the future, so we assume that no changes will take place. This is not ideal, because it is clear that changes *will* occur, and the emission height does affect the sulphate distribution, as already noted. What is required is a scenario of emission height changes consistent with the economic assumptions in the SRES scenarios. In the meantime, for $t \geq 1990$ we have

$$\frac{H(x, y, t)}{H(x, y, t) + S(x, y, t)} = \mathcal{F}(x, y).$$

	Scenario				
Year	A1	A2	A1FI	B1	B2
1990	72.6	72.6	72.6	72.6	72.6
2000	69.0	69.0	69.0	69.0	69.0
2010	87.4	74.7	80.8	59.8	68.2
2020	100.8	99.5	86.9	56.2	65.0
2030	91.4	111.9	96.1	53.5	59.9
2040	77.9	108.1	94.0	53.3	58.8
2050	64.3	105.4	80.5	51.4	57.2
2060	51.2	86.3	56.3	51.2	53.7
2070	44.9	71.7	42.6	49.2	51.9
2080	30.7	64.2	39.4	42.2	49.1
2090	29.1	61.9	39.8	33.9	48.0
2100	27.4	60.3	40.1	28.6	47.3

Table C.1: Global total SO_2 emissions in Mt(S) specified in A1FI and the four preliminary SRES marker scenarios.

Acknowledgements

This work was carried out under the UK Department of the Environment, Transport and Regions Climate Prediction Programme (PECD 7/12/37) and UK Met Office Public Meteorological Service Research Programme (MSG 2/98) with supplementary support for some experiments from the Commission of the European Communities (contract ENV4-CT95-0102 – SIDDACLICH). We thank Denise Cresswell and Gareth Jones for help in running the A1FI experiment, and Chris Colloff and Tristan Tuftnell for help with data analysis, preparing figures and tables.

References

Albrecht, B.A., 1989. Aerosols, cloud microphysics and fractional cloudiness. Science, 245, 1227–1230.

Andres, R. J. and Kasgnoc, A. D., 1998. A time-averaged inventory of subaerial volcanic sulfur emissions. J. Geophys. Res., 103, 25251–25261

Barnett T.P., K. Hasselmann, M. Chelliah, T. Delworth, G. Hegerl, P. Jones, E. Rasmussen, E. Roeckner, C. Ropelewski, B. Santer, and S. Tett, 1999. Detection and attribution of climate change: A Status report. Bull. Am. Met. Soc., 12, 2631–2659.

Boer, G.J., 1993. Climate change and the regulation of the surface moisture and energy budgets. Clim. Dyn., 8, 225–239.

Bohren, C.F., 1980. Multiple scattering of light and some of its observable consequences. Amer. J. Phys., 55, 524–533.

Bohren, C.F. and D.R. Huffman, 1983. Absorption and scattering of light by small particles. John Wiley & Sons, New York, 530pp.

Bower, K.N. and Choularton, T.W., 1992. A parametrization of the effective radius of ice free clouds for use in global climate models. Atmos. Res., 27, 305–339.

Cattle, H. and J. Crossley, 1995. Modelling Arctic climate change. Phil. Trans. R. Soc. London A352: 201–213.

Collins, M., S.F.B. Tett and C. Cooper, 2000. The internal climate variability of a version of HadCM3, a version of the Hadley Centre coupled model without flux adjustments. Clim. Dyn., 17, 61–81.

Collins, W.J., D.S. Stevenson, C.E. Johnson and R.G. Derwent, 1997. Tropospheric ozone in global-scale three-dimensional model and its response to NOx emission controls. J. Atmos. Chem., 26, 223–274.

Collins, W.J., D.S. Stevenson, C.E. Johnson and R.G. Derwent, 1999. The role of convection in determining the budget of odd hydrogen in the upper troposphere. J. Geophys. Res., 104, 26927–26941.

Cox, P., R. Betts, C. Bunton, R. Essery, P.R. Rowntree, and J. Smith, 1999. The impact of new land surface physics on the GCM simulation of climate and climate sensitivity. Clim. Dyn., 15, 183–203.

Cusack, S., A. Slingo, J.M. Edwards, and M. Wild, 1998. The radiative impact of a simple aerosol climatology on the Hadley Centre GCM. Quart. J. R. Meteor. Soc., 124, 2517–2526.

Edwards, J.M. and A. Slingo, 1996. Studies with a flexible new radiation code. I: Choosing a configuration for a large scale model. Quart. J. R. Meteor. Soc., 122, 689–719.

Fitzgerald, J.W., 1975. Approximation Formulas for the Equilibrium Size of an Aerosol Particle as a Function of Its Dry Size and Composition and the Ambient Relative Humidity. J. Applied Met., 14, 1044–1049.

Gent, P.R. and J.C. McWilliams, 1990. Isopycnal mixing in ocean circulation models. J. Phys. Oceanogr., 20: 150–155.

Gregory, D. and P.R. Rowntree, 1990. A mass flux convection scheme with representation of ensemble characteristics and stability dependent closure, Mon. Weather Rev., 118, 1483–1506.

Gregory, D., R. Kershaw and P.M. Inness, 1997. Parametrization of momentum transport by convection. II: tests in single column and general circulation models. Quart. J. R. Meteor. Soc., 123, 1153–1183.

Gregory, D., G.J. Shutts and J.R. Mitchell, 1998. A new gravity wave drag scheme incorporating anisotropic orography and low level wave breaking: Impact upon the climate of the UK Meteorological Office Unified Model. Quart. J. R. Meteor. Soc., 124, 463–493.

Gregory, J.M. and J.A. Lowe, 2000. Predictions of global and regional sea-level rise using AOGCMs with and without flux adjustment. Geophys. Res. Let., 27, 3069–3072.

Gregory, J.M., J.A. Church, G.J. Boer, K.W. Dixon, G.M. Flato, D.R. Jackett, J.A. Lowe, S.P. O'Farrell, E. Roeckner, R.J. Stouffer and M. Winton, 2001. Comparison of results from several AOGCMs for global and regional sea level change 1900 to 2100. (Submitted to Clim. Dyn.).

Gordon, C., C. Cooper, C.A. Senior, H.T. Banks, J.M. Gregory, T.C. Johns, J.F.B. Mitchell and R.A. Wood, 2000. The simulation of SST, sea ice extents and ocean heat transports in a version of the Hadley Centre coupled model without flux adjustments. Clim. Dyn., 16, 147–168.

Hough, A.M., 1991. Development of a two-dimensional global tropospheric model: model chemistry. J. Geophys. Res., 96, 7325–7326.

Houghton, J.T., G.J. Jenkins and J.J. Ephraums (eds), 1990. Climate Change: The IPCC Scientific Assessment, Cambridge University Press.

Houghton, J.T., L.G. Meira Filho, J. Bruce, H. Lee, B.A. Callander, E. Haites, N. Harris and K. Maskell (eds), 1996. Climate Change 1995: The science of climate change, Cambridge University Press.

Hulme, M. and G.J. Jenkins, 1998. Climate Change Scenarios for the United Kingdom. UK Climate Impacts Programme Tech Note 1, (61+xv)pp.

Hulme, M., J.F.B. Mitchell, W.J. Ingram, T.C. Johns, M. New and D. Viner, 1999. "Climate Change Scenarios for Global Impact Studies". Global Environmental Change, 9, S3–S19.

Johns, T.C., R.E. Carnell, J.F. Crossley, J.M. Gregory, J.F.B. Mitchell, C.A. Senior, S.F.B. Tett and R.A. Wood, 1997. The Second Hadley Centre Coupled Ocean-Atmosphere GCM: Model Description, Spinup and Validation. Clim. Dyn., 13, 103–134.

Johnson, C.E., W.J. Collins, D.S. Stevenson, and R.G. Derwent, 1999. Relative roles of climate and emissions changes on future tropospheric oxidant concentrations. J. Geophys. Res., 104, 18631–18645.

Jones, A., D.L. Roberts and A. Slingo, 1994. A climate model study of indirect radiative forcing by anthropogenic sulphate aerosols. Nature, 370, 450–453.

Jones, A., D.L. Roberts and M.J. Woodage, 1999. The indirect effects of anthropogenic sulphate aerosol simulated using a climate model with an interactive sulphur cycle. Hadley Centre Technical Note No. 14, Met Office, Bracknell, UK, 39pp.

Joos F., Bruno, M., Fink, R., Siegenthaler, U., Stocker, T., Le Quéré, C. and Sarmiento, J.L., 1996. An efficient and accurate representation of complex oceanic and biospheric models of anthropogenic carbon uptake. Tellus, 48B, 397–417.

Kattenberg, A., F. Georgi, H. Grassl, G.A. Meehl, J.F.B. Mitchell, R.J. Stouffer, T. Tokioka, A.J. Weaver and T.M.L. Wigley, 1996. Climate Models - Projections of Future Climate. In: Climate Change 1995. The Science of Climate Change. eds. Houghton, J.L., Meira Filho, L.G., Callander, B.A., Harris, N., Kattenberg, A. and Maskell, K. Cambridge University Press, UK.

Kettle, A. J., Andreae, M.O., Amouroux, D., Andreae, T.W., Bates, T.S., Berresheim, H., Bingemer, H., Boniforti, R., Helas, G., Leck, C., Maspero, M., Matari, P., McTaggart, A.R., Mihalopoulos, N., Nguyen, B.C., Novo, A., Putaud, J.P., Rapsomanikas, S., Roberts, G., Schebeske, G., Sharma, S., Simo, R., Staubes, R., Turner, S. and Uher, G., 1999. A global data base of sea surface dimethylsulfide (DMS) measurements and a procedure to predict sea surface DMS as a function of latitude, longitude and month. Global Biogeochemical Cycles, 13, 399–444.

Kraus, E.B. and J.S. Turner, 1967. A one dimensional model of the seasonal thermocline. Part II. Tellus, 19, 98–105.

Levitus, S. and T.P. Boyer, 1994: World Ocean Atlas 1994, Volume 4: Temperature. NOAA/NESDIS E/OC21, US Department of Commerce, Washington, DC, 117pp.

Levitus, S., R. Burgett, and T.P. Boyer, 1995: World Ocean Atlas 1994, Volume 3: Salinity. NOAA/NESDIS E/OC21, US Department of Commerce, Washington, DC, 99pp.

Li, D. and Shine, K.P., 1995. A 4-dimensional ozone climatology for UGAMP models. UGAMP Internal Report 35.

Liss, P. S. and Merlivat, L., 1986. Air-sea gas exchange rates: introduction and synthesis. In: The role of air-sea exchange in geochemical cycling (Ed. P. Buat-Menard). Reidel, Dordrecht

Manabe, S. and R.T. Wetherald, 1975. The effect of doubling CO_2 concentrations on the climate of a GCM. J. Atmos. Sci, 32, 3–15.

Martin, G.M., Johnson, D.W. and Spice, A., 1994. The measurement and parametrization of effective radius of droplets in warm stratocumulus clouds. J. Atmos. Sci., 51, 1823–1842.

Milton, S.F. and C.A. Wilson, 1996. The impact of parametrized sub-grid scale orographic forcing on systematic errors in a global NWP model. Mon. Weath. Rev., 124, 2023–2045.

Mitchell, J.F.B. and T.C. Johns, 1997. On modification of global warming by sulphate aerosols. J. Climate, 10, 245–267.

Mitchell, J.F.B., T.C. Johns and C.A. Senior, 1999. Transient response to increasing greenhouse gases using models with and without flux adjustments. Hadley Centre Technical Note No. 2, Met Office, Bracknell. 15pp + 20 figs.

Murphy J.M. and J.F.B. Mitchell, 1995. Transient response of the Hadley Centre coupled ocean atmosphere model to increasing carbon dioxide. Part II: Spatial and temporal structure of response. J. Climate, 8, 57–80.

Nakicenovic, N. and 27 co-authors, 2000. IPCC Special Report on Emission Scenarios. Cambridge University Press, UK, 599pp.

Olivier, J.G.J., Bouwman, A.F., van der Maas, C.W.M., Berdowski, J.J.M., Veldt, C., Bloos, J.P.J., Visschedijk, A.J.H., Zandveld, P.Y.K. and Haverlag, J.L., 1996, Description of EDGAR Version 2.0: A set of global emission inventories of greenhouse gases and ozone-depleting substances for all anthropogenic and most natural sources on a per country basis and on a 1 deg x 1 deg grid. National Institute of Public Health and the Environment, The Netherlands. RIVM report Nr. 771060 002, TNO-MEP report nr. R96/119, 141 pages.

Orn, G., U. Hansson, and H. Rodhe, 1996. Historical worldwide emissions of anthropogenic sulfur: 1860-1985. International Meteorological Institute in Stockholm, Report CM-91, Stockholm University, 5pp + 15 plates.

Pacanowski, R.C. and S.G. Philander, 1981. Parametrization of vertical mixing in numerical models of tropical oceans. J. Phys. Oceanogr., 11, 1443–1451.

Parker, D. E., P.D. Jones, C.K. Folland and A. Bevan, 1994. Interdecadal changes of surface temperature since the late nineteenth century, J. Geophys. Res., 99, 14373–14399.

Platnick, S. and Twomey, S., 1994. Determining the susceptibility of cloud albedo to changes in droplet concentration with the Advanced Very High Resolution Radiometer. J. App. Met., 33, 334–347.

Pope, V.D., M. L. Gallani, P. R. Rowntree, R. A. Stratton, 2000. The impact of new physical parametrizations in the Hadley Centre climate model: HadAM3. Clim. Dyn., 16, 123–146.

Ramanathan, V., and Dickinson, R.E., 1979. The role of stratospheric ozone in the zonal and seasonal radiative energy balance of the Earth-troposphere system. J. Atmos. Sci., 36, 1084–1104.

Randal, W.J. and Wu, F., 1999. A stratospheric ozone trends data set for global modelling studies. Geophys. Res. Lett., 26, 3089–3092.

Rayner N.A., E.B. Horton, D.E. Parker, C.K Folland and R.B. Hackett, 1996. Version 2.2 of the Global sea-Ice and Sea Surface Temperature dataset, 1903–1994. Climate Research Technical Note No. 74, Met Office, Bracknell, UK, 21pp + 13 figs.

Roeckner, E., L. Bengtsson, J. Feichter, J. Lelieveld and H. Rodhe, 1999. Transient climate change simulations with a coupled atmosphere-ocean GCM including the tropospheric sulphur cycle. J. Climate, 12, 3004–3032.

Roether, W., Roussenov, V.M. and Well, R., 1994. A tracer study sage of the thermohaline circulation of the eastern Mediterranean. In: Ocean Processes in Climate Dynamics: Global and Mediterranean Example pp.371-394. Eds. P. Malanotte-Rizzoli and A.R. Robinson, Kluwer Academic Press.

Santer, B. D., Wigley T. M. L, Barnett T. P., and Anyamba E., 1996. Detection of Climate Change and Attribution of Causes, in *Climate Change 1995. The Science of Climate Change*, eds. Houghton J. L., Meira Filho L. G., Callander B. A., Harris N., Kattenberg A., and Maskell K., Cambridge University Press, Cambridge.

Schimel, D. and 26 co-authors, 1996. Radiative forcing of climate change. In: Climate Change 1995. The Science of Climate Change. eds. Houghton, J.L., Meira Filho, L.G., Callander, B.A., Harris, N., Kattenberg, A. and Maskell, K. Cambridge University Press, UK.

Shine, K.P, R.G. Derwent, D.J. Wuebbles and J-J. Morcrette, 1990. Radiative forcing of climate. In: J.T. Houghton, G.J. Jenkins and J.J. Ephraums (eds.), Climate Change. The IPCC scientific assessment, Chapter 5, pages 45–68. Cambridge University Press, Cambridge.

Smith, R.N.B, 1990. A scheme for predicting layer clouds and their water content in a general circulation model. Quart. J. R. Meteor. Soc. 116: 435–460.

Stevenson, D.S., C.E. Johnson, W.J. Collins, R.G. Derwent and J.M. Edwards, 2000. Future estimates of tropospheric ozone radiative forcing and methane turnover - the impact of climate change. Geophys. Res. Lett., 27, 2073–2076.

Stott, P.A., S.F.B. Tett, G.S. Jones, M.R. Allen, J.F.B. Mitchell and G.J.Jenkins, 2000. External control of twentieth century temperature by natural and anthropogenic forcings. Science, 15, 2133–2137.

Stott, P.A., S.F.B. Tett, G.S. Jones, M.R. Allen, W.J. Ingram and J. F. B. Mitchell, 2001. Attribution of Twentieth Century Temperature Change to Natural and Anthropogenic Causes, Clim. Dyn., 17, 1–21.

Tett, S.F.B., P.A. Stott, M.R. Allen, W.J. Ingram and J.F.B. Mitchell, 1999. Causes of twentieth century temperature change, Nature, 399, 569–572.

Tett, S.F.B., G.S. Jones, P.A. Stott, G.S Jones, D. Hill, J.F.B.Mitchell, M.R. Allen, W.J. Ingram, T.C. Johns, C.E. Johnson, A. Jones, D.M.H. Sexton and M.J. Woodage, 2001. Estimation of natural and anthropogenic contributions to 20th century climate temperature change. (Submitted to J. Geophys. Res.).

Toon, O.B., Pollack, J.B., and Khare, B.N., 1976. The Optical Constants of Several Atmospheric Aerosol Species: Ammonium Sulphate, Aluminium Oxide, and Sodium Chloride. J. Geophys. Res., 81, 5733–5748.

US National Assessment synthesis team, 2000. Climate Change impacts on the United States. US Global Change Programme, Cambridge University Press, 154pp.

Visbeck, M., J. Marshall, T. Haine and M. Spall, 1997. On the specification of eddy transfer coefficients in coarse resolution ocean circulation models. J. Phys. Oceanogr., 27, 381–402.

Wang,H.J. D.M. Cunnold and X. Bao, 1996. A critical analysis of Stratospheric Aerosol and Gas Experiment ozone trends. J. Geophys. Res., 101, D7, 12495–12514.

White, W.B., Cayan, D.R. and Lean, J. 1998. Global upper ocean heat storage response to radiative forcing from changing solar irradiance and increasing greenhouse gas/aerosol concentrations. J. Geophys. Res., 103, 21355–21306.

Williams, K.D, C.A. Senior and J.F.B.Mitchell, 2001a. Transient climate change in the Hadley Centre models: the role of physical processes. J. Climate (accepted).

Williams, K.D., A. Jones, D.L. Roberts, C.A. Senior and M.J. Woodage, 2001b. The response of the climate system to the indirect effects of anthropogenic sulphate aerosol. Clim. Dyn. (accepted).

Wood, R.A., A.B. Keen, J.F.B. Mitchell and J.M. Gregory, 1999. Changing spatial structure of the thermohaline circulation in response to atmospheric CO_2 forcing in a climate model. Nature, 399, 572–575.

Wright, D.K., 1997. A new eddy mixing parametrization and ocean general circulation model. International WOCE newsletter, 26, 27–29.

Xie, P. and Arkin, P.A. 1997. Global precipitation: a 17-year monthly analysis based on gauge observations, satellite estimates and numerical model outputs. Bull. Amer. Met. Soc., 78, 2539–2558.

Tables

Year	CO_2 (ppmv)	CH_4 (ppbv)	N_2O (ppbv)	CFC-11 (pptv)	CFC-12 (pptv)	CFC-113 (pptv)	HCFC-22 (pptv)	HFC-125 (pptv)	HFC-134A (pptv)
1859	286.1	878	280.1	0	0	0	0	0	0
1875	288.8								
1890	294.3	947							
1900	295.9								
1917	302.2								
1920		1032							
1935	309.6								
1940		1098							
1950	310.9		290.0	0	0				
1957		1191							
1960	316.9			18	30				
1965			294.2						
1970	325.7			60	120		0		
1980	338.9			173		0			
1984			303.7						
1990	351.1	1718	310	263	477	77	91	0	0
1995	358.1								
1998				262	533	83			
2000	366.8	1762	318	251	523	81	165	2	34
2010	388.4	1874	327	206	474	72	188	5	94
2020	415.4	2012	338	169	430	64	151	10	168
2030	448.9	2170	351	138	389	57	110	16	237
2040	486.3	2353	364	113	353	51	85	23	283
2050	526.9	2559	378	93	320	45	68	32	333
2060	571.6	2783	392	76	290	40	31	42	456
2070	620.9	3026	407	62	263	36	15	53	585
2080	676.7	3295	422	51	239	32	8	66	735
2090	741.9	3593	439	42	216	28	4	81	914
2100	818.9	3927	455	34	196	25	2	99	1134

Table 1a: Greenhouse gas concentrations input to the model versus simulated year, for the historical period 1859-1990 followed by the SRES A2 scenario. Entries left blank and intermediate years are linearly interpolated from the given data points.

Year	CO_2 (ppmv)	CH_4 (ppbv)	N_2O (ppbv)	HCFC22 (pptv)	HFC125 (pptv)	HFC134A (pptv)
1990	351.1	1718	310	91	0	0
1995	358.1					
2000	366.8	1745	318	164	2	35
2010	387.9	1821	327	188	6	98
2020	410.7	1927	335	150	11	168
2030	433.0	2041	342	100	19	259
2040	454.8	2165	347	52	27	357
2050	476.9	2299	352	24	38	474
2060	499.5	2395	356	11	49	587
2070	523.2	2445	358	5	60	684
2080	547.9	2476	361	2	70	777
2090	574.8	2499	362	1	80	873
2100	603.7	2521	364	0.5	90	977

Table 1b: As Table 1a, but for the SRES B2 scenario 1990-2100. Note that the CFC concentrations (omitted) are identical to the SRES A2 case.

Year	CO_2 (ppmv)	CH_4 (ppbv)	N_2O (ppbv)	HCFC22 (pptv)	HFC125 (pptv)	HFC134A (pptv)
1990	351.1	1700	308	97	0	1
1995	358.1					
2000	366.4	1707	316	172	1	20
2010	386.9	1763	325	249	3	65
2020	414.0	1874	336	215	11	138
2030	450.5	2048	348	132	23	248
2040	497.5	2277	363	84	38	370
2050	556.0	2528	381	47	56	517
2060	623.0	2730	399	21	75	659
2070	694.5	2884	416	9	92	758
2080	770.8*	3025	433	4	105	810
2090	848.5	3155	449	2	116	832
2100	925.5	3263	465	1	123	829

Table 1c: As Table 1a, but for the SRES A1FI scenario 1990-2100. Note that the CFC concentrations (omitted) are identical to the SRES A2 case.

A2	OECD90	FSU/EE = REF	China/CPA+SE Asia = ASIA	Lat Am+Afr/Mid E = ALM	Shipping	Total
1990	22.7	17.9	11.9 + 6.0 = 17.9	4.8 + 6.3 = 11.1	3.0	72.6
2000	18.6	11.4	15.3 + 8.1 = 23.4	5.3 + 7.3 = 12.6	3.0	69.0
2010	9.4	11.5	18.4 + 16.0 = 34.4	8.2 + 8.1 = 16.3	3.0	74.7
2020	9.9	12.3	21.6 + 28.3 = 49.9	11.7 + 12.6 = 24.3	3.0	99.5
2030	10.4	12.3	20.2 + 34.7 = 54.9	12.9 + 18.4 = 31.3	3.0	111.9
2040	10.5	11.3	17.5 + 33.8 = 51.3	11.2 + 20.9 = 32.1	3.0	108.1
2050	10.6	10.5	15.1 + 32.9 = 48.0	9.7 + 23.7 = 33.4	3.0	105.4
2060	9.8	8.1	13.0 + 24.6 = 37.6	6.3 + 21.5 = 27.8	3.0	86.3
2070	9.2	6.1	11.2 + 18.4 = 29.6	4.1 + 19.7 = 23.8	3.0	71.7
2080	9.5	4.9	9.8 + 15.3 = 25.1	3.2 + 18.7 = 21.9	3.0	64.2
2090	10.6	4.0	8.6 + 14.1 = 22.7	2.9 + 18.7 = 21.6	3.0	61.9
2100	11.8	3.2	7.5 + 13.0 = 20.5	2.7 + 19.1 = 21.8	3.0	60.3
B2	OECD90	FSU/EE = REF	China/CPA+SE Asia = ASIA	Lat Am+Afr/Mid E = ALM	Shipping	Total
1990	22.7	17.9	11.9 + 6.0 = 17.9	4.8 + 6.3 = 11.1	3.0	72.6
2000	18.6	11.4	15.3 + 8.1 = 23.4	5.3 + 7.3 = 12.6	3.0	69.0
2010	13.4	9.5	18.6 + 10.7 = 29.3	5.7 + 7.3 = 13.0	3.0	68.2
2020	8.1	5.8	21.7 + 12.0 = 33.7	7.3 + 7.2 = 14.5	3.0	65.0
2030	3.9	2.4	21.6 + 13.9 = 35.5	7.1 + 8.0 = 15.1	3.0	59.9
2040	3.4	0.7	19.5 + 15.8 = 35.3	6.8 + 9.6 = 16.4	3.0	58.8
2050	3.0	0.6	17.5 + 15.7 = 33.2	6.4 + 11.0 = 17.4	3.0	57.2
2060	2.6	2.4	10.9 + 15.9 = 26.8	6.5 + 12.4 = 18.9	3.0	53.7
2070	2.7	2.5	7.8 + 16.4 = 24.2	6.0 + 13.6 = 19.6	3.0	51.9
2080	2.9	2.8	5.7 + 15.7 = 21.4	5.2 + 13.8 = 19.0	3.0	49.1
2090	3.2	3.3	5.2 + 15.0 = 20.2	4.4 + 14.1 = 18.5	3.0	48.0
2100	3.6	3.7	4.9 + 14.8 = 19.7	3.4 + 13.8 = 17.2	3.0	47.3
A1FI	OECD90	FSU/EE = REF	China/CPA+SE Asia = ASIA	Lat Am+Afr/Mid E = ALM	Shipping	Total
1990	22.7	17.0	17.7	10.5	3.0	70.9
2000	17.0	11.0	25.3	12.8	3.0	69.0
2010	13.9	10.3	38.8	14.9	3.0	80.8
2020	4.7	10.5	52.7	16.1	3.0	86.9
2030	4.0	13.3	57.1	18.6	3.0	96.1
2040	4.2	13.4	51.9	21.5	3.0	94.0
2050	5.1	10.7	37.0	24.7	3.0	80.5
2060	5.2	5.8	24.3	17.9	3.0	56.3
2070	5.7	3.1	17.0	13.8	3.0	42.6
2080	6.5	2.4	15.1	12.4	3.0	39.4
2090	7.3	2.5	14.6	12.4	3.0	39.8
2100	8.0	2.6	14.1	12.4	3.0	40.1

Table 1d: Sulphur emissions (Gt(S)/year) by world economic regions at decadal intervals in the preliminary SRES scenarios A2 and B2 (Steve Smith, personal communication), and the A1FI scenario [*Nakicenovic et al.,* 2000]. OECD90 = OECD group developed countries, FSU/EE = Former Soviet Union and Eastern Europe, CPA = Centrally Planned Asia, Lat Am = Latin America, Afr/Mid E = Africa and Middle East. The full definitions of the world regions are given on pages 332-333 of *Nakicenovic et al.,* 2000. Note that the emissions used in the HadCM3 A1FI experiment at 1990 were identical to those used in A2 and B2 for simplicity rather than the values tabulated above.

Forcings (W/m^2)	GHGs	Sulphate (Direct)	Sulphate (Indirect)	Ozone (Trop)	Ozone (Strat)
HadCM3 B2 (2000)	2.27	-0.18	-0.91	0.35	-0.14
IPCC 1995	[2.1,2.8]	[-0.2,-0.8]	[0.0,-1.5]	[0.2,0.6]	[-0.05,-0.2]

Table 2: Comparison of HadCM3 global mean present day (2000) forcing relative to pre-industrial values with IPCC 1995 [*Schimel,* 1996] estimated ranges for present day. HadCM3 figures are from the B2 experiment. Stratospheric ozone forcing at 2000 is estimated by extrapolation from 1990 and 1998 values.

GLOBAL MEANS - 2040s	CTL	G92	GB2	B2	A2	A1FI
TOP OF ATMOSPHERE	$[W/m^2]$					
SW at toa (down)	341.41					
SW at toa (up)	-100.99	1.86	1.79	0.55	0.40	0.67
SW at toa (up - CS)	-51.34	1.49	1.44	0.78	0.64	0.91
SW at toa (net)	240.42	1.86	1.79	0.55	0.40	0.67
SW cloud forcing	-49.65	0.37	0.35	-0.24	-0.25	-0.23
LW at toa (up net)	-240.59	-0.62	-0.75	0.47	0.80	0.70
LW at toa (up - CS)	-262.16	-0.22	-0.36	1.03	1.45	1.34
LW cloud forcing	21.57	-0.40	-0.39	-0.56	-0.65	-0.64
Net radiation at toa	-0.17	1.24	1.03	1.02	1.19	1.37
Net cloud forcing	-28.07	-0.03	-0.04	-0.80	-0.90	-0.88
TROPOPAUSE FLUXES	$[W/m^2]$					
SW at trop (net)	227.33	2.05	1.68	0.56	0.37	0.65
SW at trop (upwards)	-100.56	1.89	1.75	0.54	0.39	0.67
LW at trop (net)	-225.47	-0.92	-0.72	0.36	0.73	0.61
LW at trop (downwards)	16.28	0.47	0.65	0.30	0.42	0.42
Net radiation at trop	1.86	1.12	0.95	0.92	1.10	1.26
STRATOSPHERIC HEATING	$[W/m^2]$					
Strat. rad. heating	-2.04	0.12	0.08	0.10	0.10	0.11
SURFACE FLUXES	$[W/m^2]$					
SW (reflected)	-24.31	1.26	1.12	0.98	1.10	1.19
SW (net)	164.34	-0.07	-0.24	-1.07	-1.39	-1.38
LW (emitted)	-394.87	-12.60	-11.27	-8.59	-9.45	-10.48
LW (net)	-62.63	3.79	3.49	3.34	3.72	4.13
Surface net radiation	101.71	3.72	3.25	2.28	2.33	2.75
Sensible heat	-16.98	0.01	0.07	0.12	0.12	0.10
Latent heat	-84.15	-2.62	-2.39	-1.46	-1.35	-1.60
Surface net heat flux	0.57	1.12	0.93	0.94	1.09	1.25
ATMOSPHERIC HEATING	$[W/m^2]$					
Atmos. radiative heating	-101.88	-2.49	-2.22	-1.26	-1.14	-1.38
Atmos. greenhouse effect	154.28	11.98	10.51	9.06	10.25	11.18
HYDROLOGY	$[mm/day]$					
Total rainfall	2.686	0.121	0.109	0.071	0.068	0.080
Total snowfall	0.217	-0.030	-0.026	-0.021	-0.022	-0.025
Total precipitation	2.903	0.091	0.083	0.051	0.047	0.055
Dynamic precip	0.723	0.021	0.020	0.013	0.015	0.017
Convective precip	2.180	0.069	0.062	0.038	0.032	0.038
Evaporation+sublim	2.904	0.091	0.083	0.051	0.047	0.056
Atmos moisture source	-0.002	0.000	0.000	0.000	0.000	0.000
SURFACE AIR TEMPERATURE	[K]					
Temperature at 1.5m	286.65	2.43	2.17	1.66	1.83	2.03

Table 3a: Global mean fluxes and energy budget terms in the control run (CTL) and the corresponding differences in the forced experiments relative to the control run for the 2040s period. Positive fluxes indicate a net downwards flux or into the layer considered.

LAND-ONLY MEANS - 2040s	CTL	G92	GB2	B2	A2	A1FI
TOP OF ATMOSPHERE	$[W/m^2]$					
SW at toa (down)	326.87					
SW at toa (up)	-112.35	4.41	4.08	1.83	1.66	2.23
SW at toa (up - CS)	-77.75	1.89	1.82	0.88	0.57	0.95
SW at toa (net)	214.53	4.41	4.08	1.83	1.66	2.23
SW cloud forcing	-34.60	2.51	2.26	0.95	1.09	1.28
LW at toa (up net)	-233.94	-2.61	-2.40	-0.80	-0.55	-0.83
LW at toa (up - CS)	-251.54	-2.44	-2.28	-0.42	-0.09	-0.45
LW cloud forcing	17.60	-0.17	-0.12	-0.37	-0.47	-0.38
Net radiation at toa	-19.41	1.80	1.68	1.03	1.11	1.39
Net cloud forcing	-17.00	2.35	2.14	0.58	0.63	0.89
TROPOPAUSE FLUXES	$[W/m^2]$					
SW at trop (net)	201.49	4.61	4.00	1.89	1.68	2.26
SW at trop (upwards)	-112.03	4.48	4.09	1.86	1.70	2.26
LW at trop (net)	-217.94	-3.03	-2.47	-0.98	-0.69	-1.01
LW at trop (downwards)	17.05	0.44	0.65	0.26	0.40	0.37
Net radiation at trop	-16.45	1.58	1.53	0.91	1.00	1.25
STRATOSPHERIC HEATING	$[W/m^2]$					
Strat. rad. heating	-2.96	0.22	0.14	0.12	0.11	0.15
SURFACE FLUXES	$[W/m^2]$					
SW (reflected)	-51.33	1.20	1.08	1.07	1.17	1.28
SW (net)	139.75	2.87	2.44	0.56	0.31	0.59
LW (emitted)	-366.71	-18.18	-16.15	-12.36	-13.46	-15.24
LW (net)	-68.53	0.39	0.41	1.07	1.24	1.40
Surface net radiation	71.22	3.26	2.85	1.63	1.55	1.99
Sensible heat	-29.46	-4.02	-3.52	-2.68	-3.08	-3.41
Latent heat	-41.08	0.77	0.67	1.06	1.57	1.45
Surface net heat flux	0.68	0.01	0.00	0.02	0.03	0.04
ATMOSPHERIC HEATING	$[W/m^2]$					
Atmos. radiative heating	-90.63	-1.46	-1.17	-0.60	-0.44	-0.60
Atmos. greenhouse effect	132.77	15.57	13.75	11.56	12.91	14.40
HYDROLOGY	$[mm/day]$					
Total rainfall	1.842	0.068	0.067	0.007	-0.012	0.019
Total snowfall	0.284	-0.020	-0.016	-0.010	-0.009	-0.011
Total precipitation	2.126	0.048	0.050	-0.003	-0.020	0.008
Dynamic precip	0.567	0.015	0.014	0.005	0.006	0.012
Convective precip	1.559	0.033	0.036	-0.008	-0.026	-0.004
Evaporation+sublim	1.413	-0.025	-0.022	-0.036	-0.054	-0.050
Atmos moisture source	0.713	0.074	0.073	0.034	0.033	0.058
SURFACE AIR TEMPERATURE	[K]					
Temperature at 1.5m	280.29	3.44	3.05	2.34	2.56	2.88

Table 3b: As Table 3a but means over land points only.

SEA-ONLY MEANS - 2040s	CTL	G92	GB2	B2	A2	A1FI
TOP OF ATMOSPHERE	$[W/m^2]$					
SW at toa (down)	347.33					
SW at toa (up)	-96.36	0.82	0.85	0.02	-0.12	0.04
SW at toa (up - CS)	-40.58	1.32	1.28	0.74	0.67	0.89
SW at toa (net)	250.97	0.82	0.85	0.02	-0.12	0.04
SW cloud forcing	-55.78	-0.50	-0.43	-0.72	-0.79	-0.85
LW at toa (up net)	-243.30	0.19	-0.08	0.99	1.35	1.32
LW at toa (up - CS)	-266.49	0.68	0.42	1.63	2.08	2.07
LW cloud forcing	23.19	-0.49	-0.50	-0.64	-0.73	-0.75
Net radiation at toa	7.67	1.01	0.77	1.01	1.23	1.36
Net cloud forcing	-32.59	-1.00	-0.93	-1.36	-1.52	-1.60
TROPOPAUSE FLUXES	$[W/m^2]$					
SW at trop (net)	237.87	1.00	0.73	0.02	-0.16	-0.01
SW at trop (upwards)	-95.89	0.83	0.80	0.00	-0.14	0.01
LW at trop (net)	-228.54	-0.06	-0.01	0.91	1.30	1.27
LW at trop (downwards)	15.97	0.48	0.65	0.32	0.42	0.43
Net radiation at trop	9.33	0.94	0.71	0.93	1.14	1.27
STRATOSPHERIC HEATING	$[W/m^2]$					
Strat. rad. heating	-1.66	0.07	0.06	0.09	0.09	0.09
SURFACE FLUXES	$[W/m^2]$					
SW (reflected)	-13.30	1.28	1.13	0.94	1.08	1.15
SW (net)	174.36	-1.27	-1.33	-1.73	-2.08	-2.19
LW (emitted)	-406.35	-10.32	-9.28	-7.05	-7.82	-8.54
LW (net)	-60.22	5.18	4.74	4.27	4.73	5.25
Surface net radiation	114.13	3.91	3.42	2.54	2.65	3.05
Sensible heat	-11.90	1.65	1.53	1.26	1.42	1.53
Latent heat	-101.70	-4.00	-3.64	-2.49	-2.55	-2.84
Surface net heat flux	0.53	1.57	1.31	1.32	1.53	1.75
ATMOSPHERIC HEATING	$[W/m^2]$					
Atmos. radiative heating	-106.47	-2.90	-2.64	-1.53	-1.42	-1.69
Atmos. greenhouse effect	163.04	10.51	9.19	8.04	9.17	9.86
HYDROLOGY	$[mm/day]$					
Total rainfall	3.030	0.142	0.126	0.097	0.101	0.105
Total snowfall	0.190	-0.034	-0.030	-0.025	-0.027	-0.031
Total precipitation	3.219	0.108	0.096	0.072	0.074	0.074
Dynamic precip	0.786	0.024	0.023	0.016	0.019	0.020
Convective precip	2.433	0.084	0.073	0.056	0.055	0.055
Evaporation+sublim	3.512	0.138	0.126	0.086	0.088	0.098
Atmos moisture source	-0.293	-0.031	-0.030	-0.014	-0.014	-0.024
SURFACE AIR TEMPERATURE	[K]					
Temperature at 1.5m	289.24	2.01	1.81	1.39	1.54	1.68

Table 3c: As Table 3a but means over sea points only.

GLOBAL MEANS - 2080s	CTL	G92	GB2	B2	A2	A1FI
TOP OF ATMOSPHERE	$[W/m^2]$					
SW at toa (down)	341.41					
SW at toa (up)	-100.99	2.58	2.31	1.52	1.98	2.81
SW at toa (up - CS)	-51.34	2.17	1.95	1.54	1.97	2.52
SW at toa (net)	240.42	2.58	2.31	1.52	1.98	2.81
SW cloud forcing	-49.65	0.41	0.36	-0.02	0.01	0.29
LW at toa (up net)	-240.59	-1.00	-1.05	-0.28	-0.08	-0.58
LW at toa (up - CS)	-262.16	-0.66	-0.75	0.24	0.62	0.05
LW cloud forcing	21.57	-0.34	-0.29	-0.52	-0.70	-0.62
Net radiation at toa	-0.17	1.58	1.26	1.24	1.91	2.23
Net cloud forcing	-28.07	0.07	0.07	-0.54	-0.69	-0.33
TROPOPAUSE FLUXES	$[W/m^2]$					
SW at trop (net)	227.33	2.68	2.13	1.19	1.58	2.39
SW at trop (upwards)	-100.56	2.58	2.25	1.44	1.90	2.72
LW at trop (net)	-225.47	-1.28	-0.99	-0.08	0.14	-0.39
LW at trop (downwards)	16.28	0.84	0.92	0.86	1.16	1.25
Net radiation at trop	1.86	1.41	1.14	1.11	1.72	2.00
STRATOSPHERIC HEATING	$[W/m^2]$					
Strat. rad. heating	-2.04	0.18	0.12	0.12	0.18	0.23
SURFACE FLUXES	$[W/m^2]$					
SW (reflected)	-24.31	1.76	1.49	1.45	1.86	2.10
SW (net)	164.34	-0.69	-0.64	-1.38	-1.85	-1.81
LW (emitted)	-394.87	-19.32	-15.94	-14.10	-18.69	-22.53
LW (net)	-62.63	5.84	4.82	4.83	6.42	7.38
Surface net radiation	101.71	5.15	4.18	3.45	4.57	5.58
Sensible heat	-16.98	-0.19	-0.19	-0.13	-0.12	-0.32
Latent heat	-84.15	-3.55	-2.87	-2.22	-2.71	-3.23
Surface net heat flux	0.57	1.41	1.12	1.11	1.74	2.02
ATMOSPHERIC HEATING	$[W/m^2]$					
Atmos. radiative heating	-101.88	-3.57	-2.92	-2.22	-2.66	-3.34
Atmos. greenhouse effect	154.28	18.32	14.90	13.81	18.61	21.96
HYDROLOGY	$[mm/day]$					
Total rainfall	2.686	0.168	0.137	0.110	0.137	0.162
Total snowfall	0.217	-0.045	-0.038	-0.033	-0.043	-0.050
Total precipitation	2.903	0.123	0.099	0.077	0.094	0.112
Dynamic precip	0.723	0.029	0.025	0.020	0.025	0.026
Convective precip	2.180	0.094	0.075	0.057	0.069	0.085
Evaporation+sublim	2.904	0.124	0.100	0.077	0.095	0.113
Atmos moisture source	-0.002	0.000	0.000	0.000	-0.001	-0.001
SURFACE AIR TEMPERATURE	[K]					
Temperature at 1.5m	286.65	3.67	3.04	2.70	3.56	4.26

Table 3d: As Table 3a but differences for the 2080s period.

LAND-ONLY MEANS - 2080s	CTL	G92	GB2	B2	A2	A1FI
TOP OF ATMOSPHERE	$[W/m^2]$					
SW at toa (down)	326.87					
SW at toa (up)	-112.35	6.60	5.92	4.23	5.43	7.14
SW at toa (up - CS)	-77.75	2.91	2.55	1.90	2.53	3.38
SW at toa (net)	214.53	6.60	5.92	4.23	5.43	7.14
SW cloud forcing	-34.60	3.69	3.37	2.33	2.90	3.76
LW at toa (up net)	-233.94	-4.10	-3.74	-2.66	-3.05	-4.26
LW at toa (up - CS)	-251.54	-4.02	-3.62	-2.22	-2.63	-3.95
LW cloud forcing	17.60	-0.08	-0.12	-0.43	-0.42	-0.31
Net radiation at toa	-19.41	2.50	2.19	1.58	2.38	2.88
Net cloud forcing	-17.00	3.61	3.26	1.90	2.48	3.45
TROPOPAUSE FLUXES	$[W/m^2]$					
SW at trop (net)	201.49	6.74	5.80	3.91	5.05	6.76
SW at trop (upwards)	-112.03	6.68	5.94	4.21	5.41	7.13
LW at trop (net)	-217.94	-4.55	-3.82	-2.56	-2.97	-4.28
LW at trop (downwards)	17.05	0.84	0.92	0.86	1.16	1.21
Net radiation at trop	-16.45	2.19	1.98	1.36	2.09	2.48
STRATOSPHERIC HEATING	$[W/m^2]$					
Strat. rad. heating	-2.96	0.31	0.21	0.22	0.29	0.40
SURFACE FLUXES	$[W/m^2]$					
SW (reflected)	-51.33	1.83	1.50	1.52	2.06	2.37
SW (net)	139.75	3.90	3.58	1.87	2.31	3.32
LW (emitted)	-366.71	-28.37	-23.39	-20.44	-27.49	-33.63
LW (net)	-68.53	0.66	0.17	0.87	1.32	1.15
Surface net radiation	71.22	4.57	3.75	2.75	3.62	4.47
Sensible heat	-29.46	-6.66	-5.74	-5.05	-6.66	-8.35
Latent heat	-41.08	2.12	2.00	2.33	3.09	3.93
Surface net heat flux	0.68	0.02	0.01	0.02	0.05	0.05
ATMOSPHERIC HEATING	$[W/m^2]$					
Atmos. radiative heating	-90.63	-2.07	-1.56	-1.17	-1.24	-1.60
Atmos. greenhouse effect	132.77	24.26	19.66	17.78	24.44	29.37
HYDROLOGY	$[mm/day]$					
Total rainfall	1.842	0.090	0.044	-0.002	0.037	0.047
Total snowfall	0.284	-0.030	-0.023	-0.016	-0.024	-0.032
Total precipitation	2.126	0.060	0.021	-0.017	0.013	0.014
Dynamic precip	0.567	0.018	0.016	0.011	0.014	0.014
Convective precip	1.559	0.042	0.005	-0.029	-0.001	0.000
Evaporation+sublim	1.413	-0.072	-0.068	-0.080	-0.105	-0.134
Atmos moisture source	0.713	0.131	0.089	0.062	0.119	0.148
SURFACE AIR TEMPERATURE	[K]					
Temperature at 1.5m	280.29	5.27	4.38	3.83	5.10	6.20

Table 3e: As Table 3b but differences for the 2080s period.

SEA-ONLY MEANS - 2080s	CTL	G92	GB2	B2	A2	A1FI
TOP OF ATMOSPHERE	$[W/m^2]$					
SW at toa (down)	347.33					
SW at toa (up)	-96.36	0.94	0.84	0.41	0.58	1.05
SW at toa (up - CS)	-40.58	1.87	1.70	1.39	1.75	2.17
SW at toa (net)	250.97	0.94	0.83	0.41	0.58	1.05
SW cloud forcing	-55.78	-0.93	-0.87	-0.98	-1.17	-1.13
LW at toa (up net)	-243.30	0.27	0.05	0.69	1.14	0.93
LW at toa (up - CS)	-266.49	0.72	0.41	1.24	1.94	1.67
LW cloud forcing	23.19	-0.45	-0.36	-0.56	-0.81	-0.75
Net radiation at toa	7.67	1.21	0.89	1.10	1.71	1.97
Net cloud forcing	-32.59	-1.38	-1.23	-1.54	-1.98	-1.87
TROPOPAUSE FLUXES	$[W/m^2]$					
SW at trop (net)	237.87	1.03	0.64	0.08	0.17	0.61
SW at trop (upwards)	-95.89	0.91	0.75	0.32	0.47	0.93
LW at trop (net)	-228.54	0.05	0.16	0.93	1.41	1.20
LW at trop (downwards)	15.97	0.85	0.91	0.86	1.16	1.27
Net radiation at trop	9.33	1.09	0.80	1.01	1.57	1.80
STRATOSPHERIC HEATING	$[W/m^2]$					
Strat. rad. heating	-1.66	0.12	0.08	0.09	0.14	0.17
SURFACE FLUXES	$[W/m^2]$					
SW (reflected)	-13.30	1.73	1.49	1.42	1.77	1.99
SW (net)	174.36	-2.56	-2.35	-2.70	-3.55	-3.90
LW (emitted)	-406.35	-15.64	-12.90	-11.51	-15.10	-18.01
LW (net)	-60.22	7.95	6.71	6.45	8.50	9.92
Surface net radiation	114.13	5.39	4.36	3.74	4.95	6.02
Sensible heat	-11.90	2.45	2.06	1.88	2.55	2.95
Latent heat	-101.70	-5.86	-4.85	-4.07	-5.08	-6.15
Surface net heat flux	0.53	1.98	1.57	1.55	2.43	2.82
ATMOSPHERIC HEATING	$[W/m^2]$					
Atmos. radiative heating	-106.47	-4.18	-3.47	-2.65	-3.24	-4.05
Atmos. greenhouse effect	163.04	15.90	12.96	12.20	16.24	18.94
HYDROLOGY	$[mm/day]$					
Total rainfall	3.030	0.200	0.175	0.155	0.177	0.208
Total snowfall	0.190	-0.051	-0.044	-0.040	-0.050	-0.057
Total precipitation	3.219	0.149	0.131	0.115	0.127	0.151
Dynamic precip	0.786	0.033	0.028	0.024	0.030	0.031
Convective precip	2.433	0.116	0.103	0.092	0.097	0.120
Evaporation+sublim	3.512	0.203	0.168	0.141	0.176	0.213
Atmos moisture source	-0.293	-0.054	-0.037	-0.026	-0.049	-0.062
SURFACE AIR TEMPERATURE	[K]					
Temperature at 1.5m	289.24	3.02	2.49	2.24	2.93	3.47

Table 3f: As Table 3c but differences for the 2080s period.

Changes from control (2040s)	G92	GHG(R99)
Surface temperature (K)	2.46	2.39
Precipitation (%)	3.1	1.62
Net TOA heating (W/m^2)	1.2	1.4
Solar cloud forcing(W/m^2)	0.4	-1.4
Surface sensible heat (W/m^2)	0.0	0.7
Surface latent heat (W/m^2)	-2.6	-1.4
Surface radiative heating (W/m^2)	3.7	2.2
Atmospheric radiative cooling (W/m^2)	-2.5	-0.8

Table 4: Comparison of the climate response in the 2040s period for the HadCM3 G92 experiment against the similar scenario experiment GHG(R99) conducted with the ECHAM4-OPYC model [*Roeckner et al.,* 1999].

Region	Period	G92	GB2	B2	A2	A1FI	B2-A2	B2-GB2	S.Dev
Globe	2040s	1.56	1.33	1.18	1.35	1.58	-0.16	-0.15	0.04
	2080s	2.80	2.20	2.22	3.07	3.81	-0.85	0.01*	
Mid-USA	2040s	2.40	1.89	1.86	2.08	2.89	-0.21*	-0.03*	0.22
	2080s	4.39	3.41	3.37	4.88	6.61	-1.51	-0.03*	
S.Europe	2040s	2.12	1.67	1.79	1.74	2.20	0.05*	0.11*	0.13
	2080s	3.70	2.73	2.94	4.24	5.43	-1.30	0.21*	
Sahel	2040s	1.95	1.78	1.59	1.79	2.08	-0.21	-0.19*	0.07
	2080s	3.80	2.95	3.01	4.20	5.13	-1.19	0.06*	
S.Asia	2040s	1.69	1.47	1.25	1.37	1.65	-0.12*	-0.22	0.07
	2080s	3.19	2.43	2.41	3.36	4.12	-0.95	-0.03*	
Australia	2040s	1.50	1.30	1.20	1.40	1.53	-0.20	-0.10*	0.05
	2080s	2.77	2.19	2.05	3.02	3.61	-0.97	-0.14	

Table 5a: Climate change signals for the globe and five selected regions for annual mean near surface temperature (K) in various HadCM3 experiments for the periods 2029-2059 (2040s) and 2069-2099 (2080s) relative to their respective 1969-1999 period. Standard deviations computed between eight successive 30 year periods from the control run are listed in the final column. Signals marked * are not significant at the 95% level assuming a normal distribution for each signal with an expected mean of zero and variance twice the square of the standard deviation from the control run (twice to account for the fact that each signal is a difference of two 30 year means). Regions are defined as in the IPCC 1990 and 1995 reports, eg. *Kattenberg et al.,* 1996.

Region	Period	G92	GB2	B2	A2	A1FI	B2-A2	B2-GB2	S.dev
Globe	2040s	0.06	0.04	0.03	0.03	0.04	0.00*	-0.01*	0.004
	2080s	0.09	0.06	0.06	0.08	0.10	-0.01	0.00*	
Mid-USA	2040s	0.11*	0.10*	-0.08*	0.18	0.04*	-0.25	-0.17	0.052
	2080s	0.12*	0.17	0.11*	0.20	0.27	-0.09*	-0.06*	
S.Europe	2040s	-0.02*	-0.06*	0.15*	-0.02*	0.05*	0.17*	0.21*	0.093
	2080s	0.05*	0.04*	0.30	0.14*	0.22*	0.16*	0.26	
Sahel	2040s	-0.01*	0.00*	0.00*	0.01*	-0.00*	-0.01*	0.00*	0.008
	2080s	0.00*	0.00*	0.01*	0.00*	-0.00*	0.01*	0.01*	
S.Asia	2040s	-0.25	-0.39	-0.26	-0.33	-0.11*	0.07*	0.13*	0.083
	2080s	-0.38	-0.42	-0.41	-0.35	-0.01*	-0.06*	0.01*	
Australia	2040s	-0.10*	-0.19*	-0.26*	-0.05*	0.08*	-0.21*	-0.07*	0.103
	2080s	-0.28*	-0.51	-0.23*	-0.20*	-0.09*	-0.02*	0.28*	

Table 5b: As Table 5a but for December-January-February (DJF) mean precipitation signals (mm/day).

Region	Period	G92	GB2	B2	A2	A1FI	B2-A2	B2-GB2	S.dev
Globe	2040s	0.06	0.05	0.05	0.04	0.04	0.01*	0.00*	0.004
	2080s	0.08	0.06	0.07	0.08	0.09	-0.01	0.01	
Mid-USA	2040s	-0.13	-0.29	-0.26	-0.18	-0.33	-0.08*	0.03*	0.033
	2080s	-0.41	-0.52	-0.24	-0.43	-0.48	0.19	0.29	
S.Europe	2040s	-0.20	-0.27	-0.23	-0.27	-0.33	0.04*	0.04*	0.036
	2080s	-0.43	-0.37	-0.35	-0.51	-0.65	0.16	0.02*	
Sahel	2040s	0.21	0.17*	0.22	0.16*	0.16*	0.06*	0.05*	0.068
	2080s	-0.04*	-0.06*	0.11*	0.06*	-0.05*	0.05*	0.17*	
S.Asia	2040s	0.62	0.67	0.43	0.50	0.71	-0.06*	-0.23*	0.096
	2080s	0.81	0.83	0.86	1.13	1.76	-0.27	0.03*	
Australia	2040s	-0.06*	0.08*	0.01*	-0.05*	-0.00*	0.06*	-0.07*	0.037
	2080s	-0.06*	-0.02*	-0.10*	-0.06*	-0.16	-0.04*	-0.08*	

Table 5c: As Table 5b but for June-July-August (JJA) mean precipitation signals (mm/day).

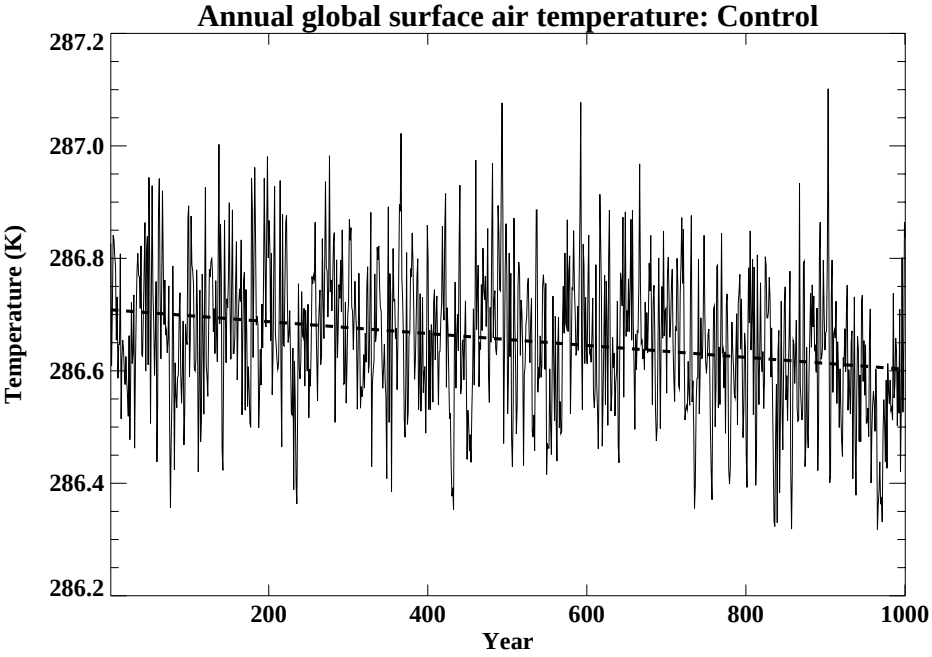

Figure 1: Timeseries of annual global mean surface air temperature over the first 1000 years of the HadCM3 control simulation. The best fit linear trend is the dashed line.

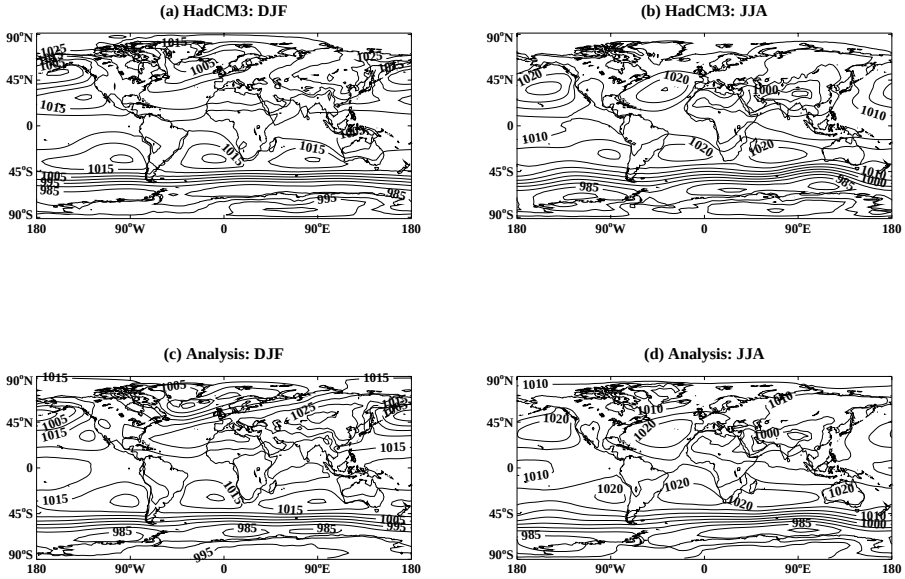

Figure 2: Seasonal average (DJF and JJA) mean sea level pressure (hPa) simulated for years 371-600 in the HadCM3 control run, compared with mean UK Met Office operational analyses for the period May 1983 to September 1995.

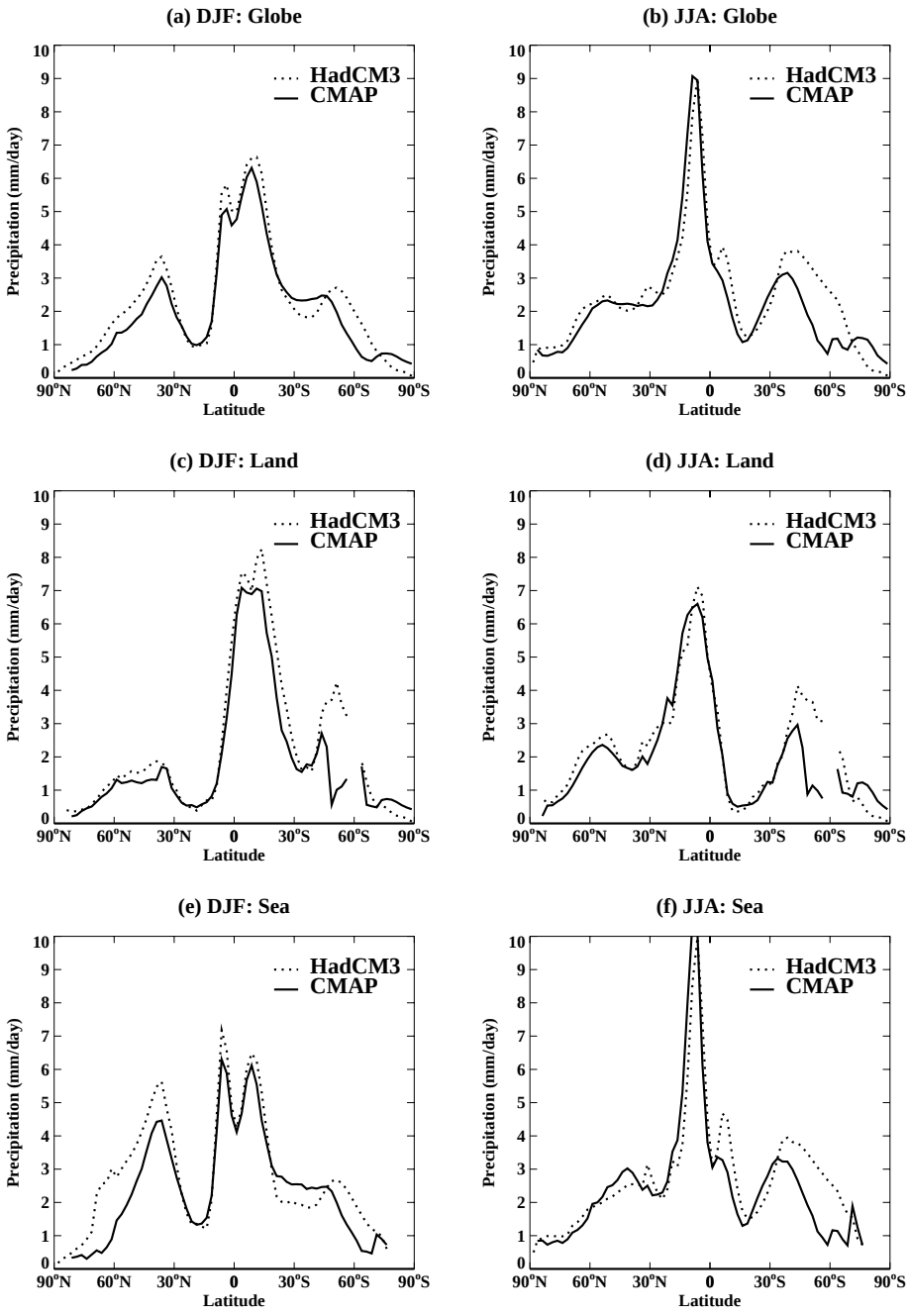

Figure 3: Zonal seasonal average (DJF and JJA) precipitation (mm/day) as simulated in the HadCM3 control run for the same period as in Figure 2 compared to the CMAP climatology [*Xie and Arkin,* 1997], for the globe, land and sea separately.

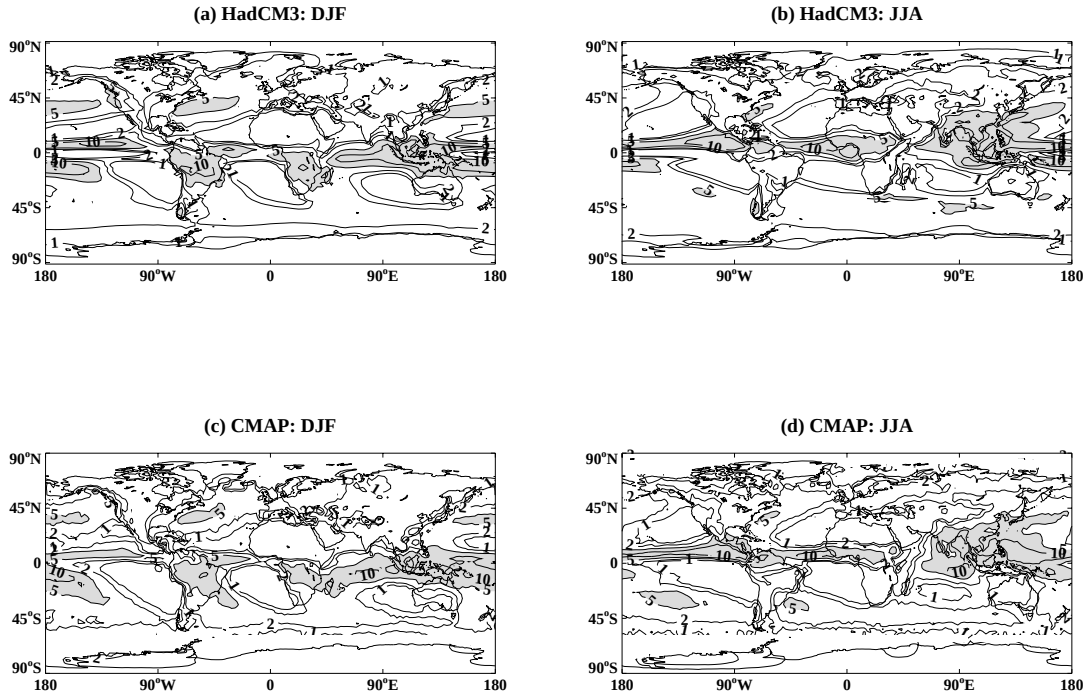

Figure 4: Seasonal average (DJF and JJA) precipitation (mm/day) in the HadCM3 control run for the same period as in Figure 2, compared with the CMAP climatology [*Xie and Arkin,* 1997]. Values above 5 mm/day are shaded.

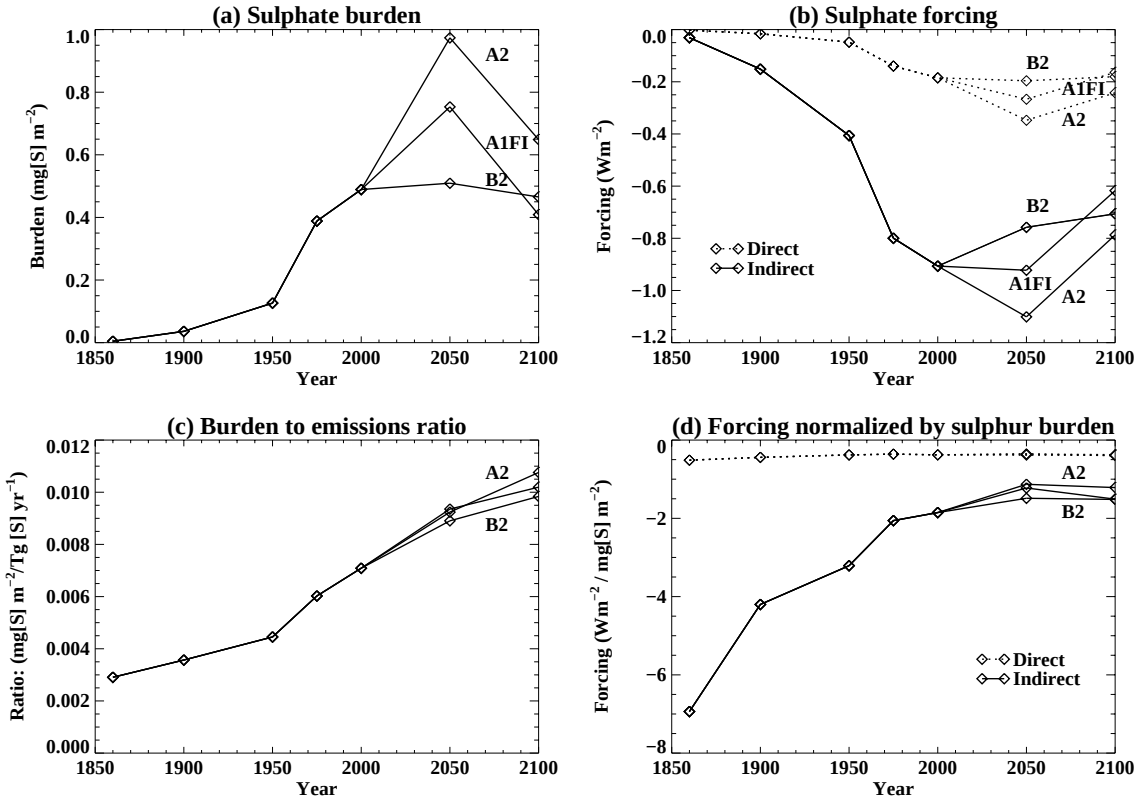

Figure 5: Timeseries of (a) global mean anthropogenic sulphate burden; (b) direct and indirect sulphate forcing; (c) ratio of sulphur burden to emissions; and (d) normalized direct and indirect forcing (i.e. forcing divided by burden); for the A2, B2 and A1FI experiments. Note that these represent data computed from re-runs of single individual years of the experiments only, not continuously throughout the simulations. Note that the indirect forcing here as diagnosed in the model is about 30% less than that diagnosed in separate calculations.

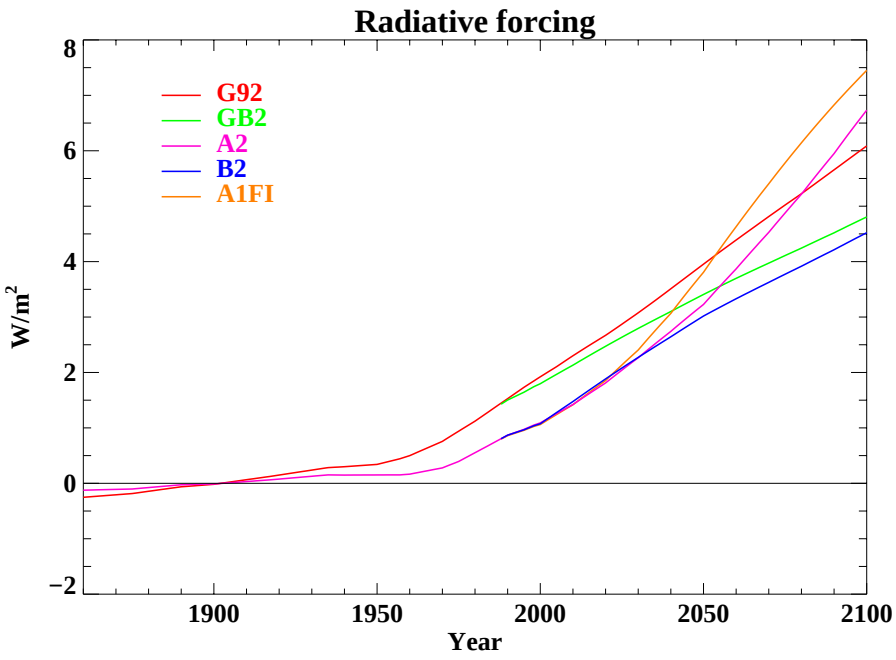

Figure 6: Timeseries of annual global mean total forcing of the troposphere computed for the HadCM3 experiments G92, GB2, A2, B2 and A1FI over the period 1859-2100, each relative to their average over the period 1880-1920. Effects of greenhouse gases, direct and indirect sulphate aerosol forcing, tropospheric and stratospheric ozone changes are included.

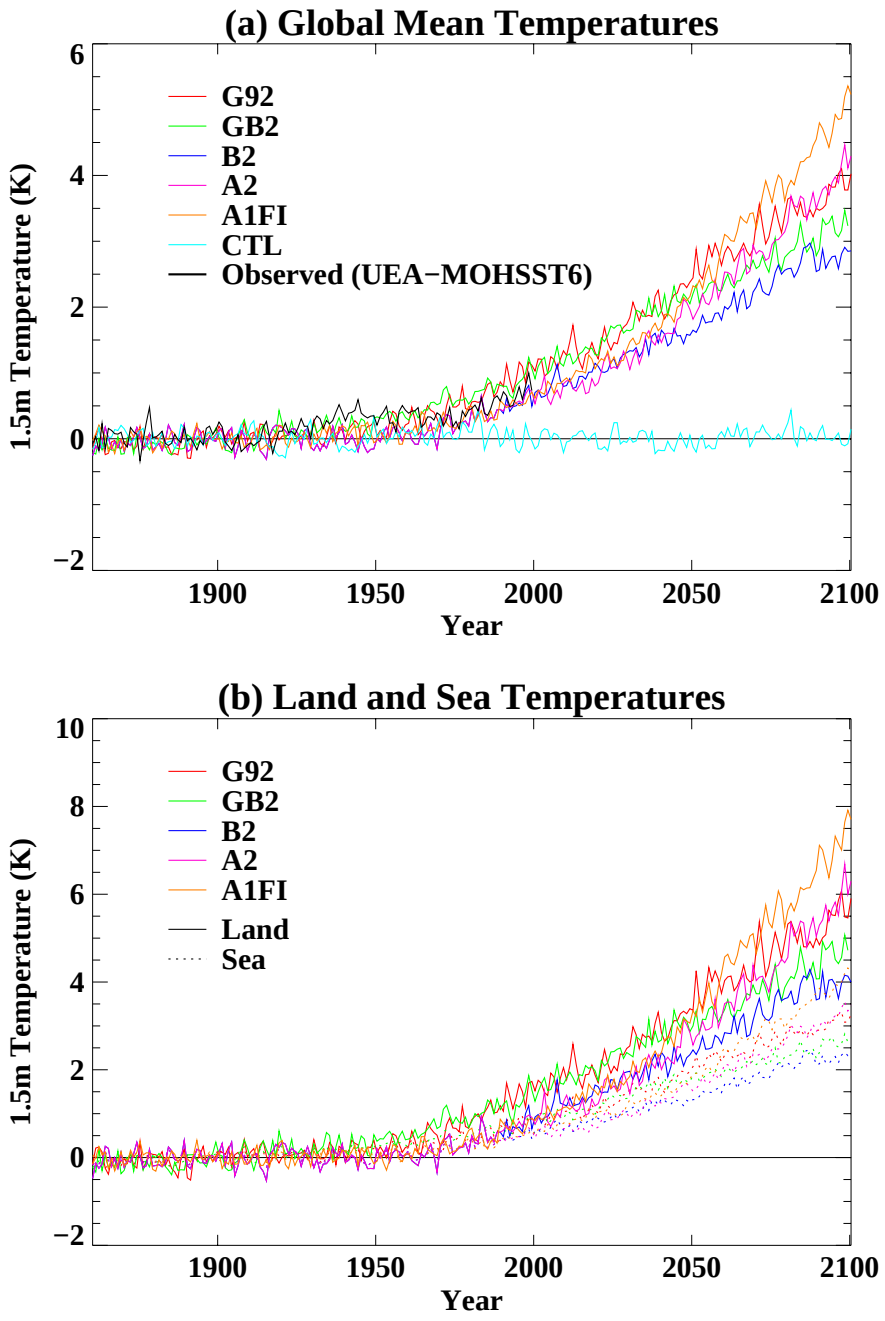

Figure 7: (a) Timeseries of annual global mean temperatures in G92, GB2, A2, B2, A1FI and CTL for the period 1859-2100, each relative to their average over the period 1880-1920. Observed global mean temperature anomalies from the MOHSST6-UEA dataset [*Parker et al.*, 1994] are also shown. (b) Timeseries of land and sea temperatures as (a) but omitting CTL and observations.

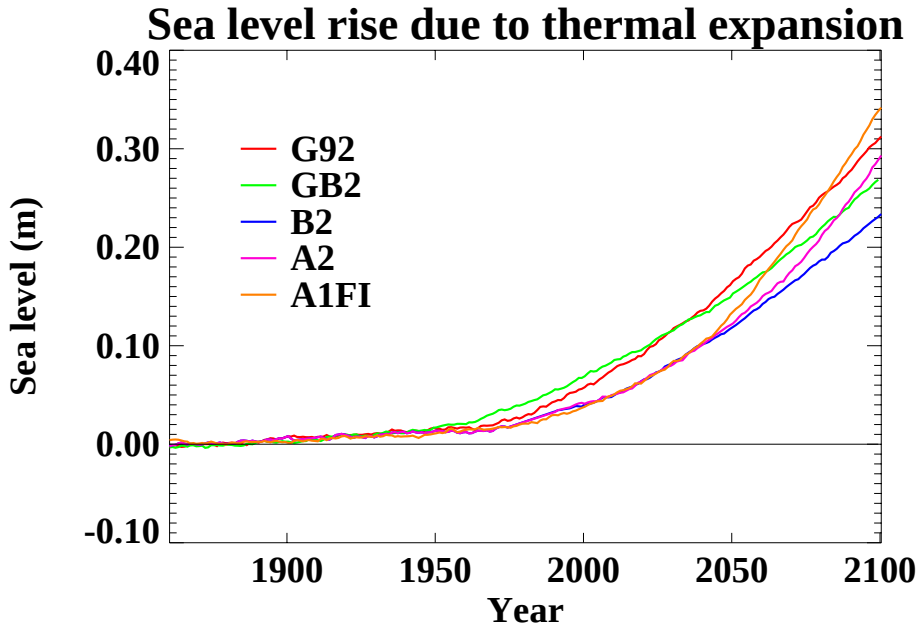

Figure 8: Timeseries of annual mean sea level rise due to thermal expansion in G92, GB2, B2, A2 and A1FI relative to CTL.

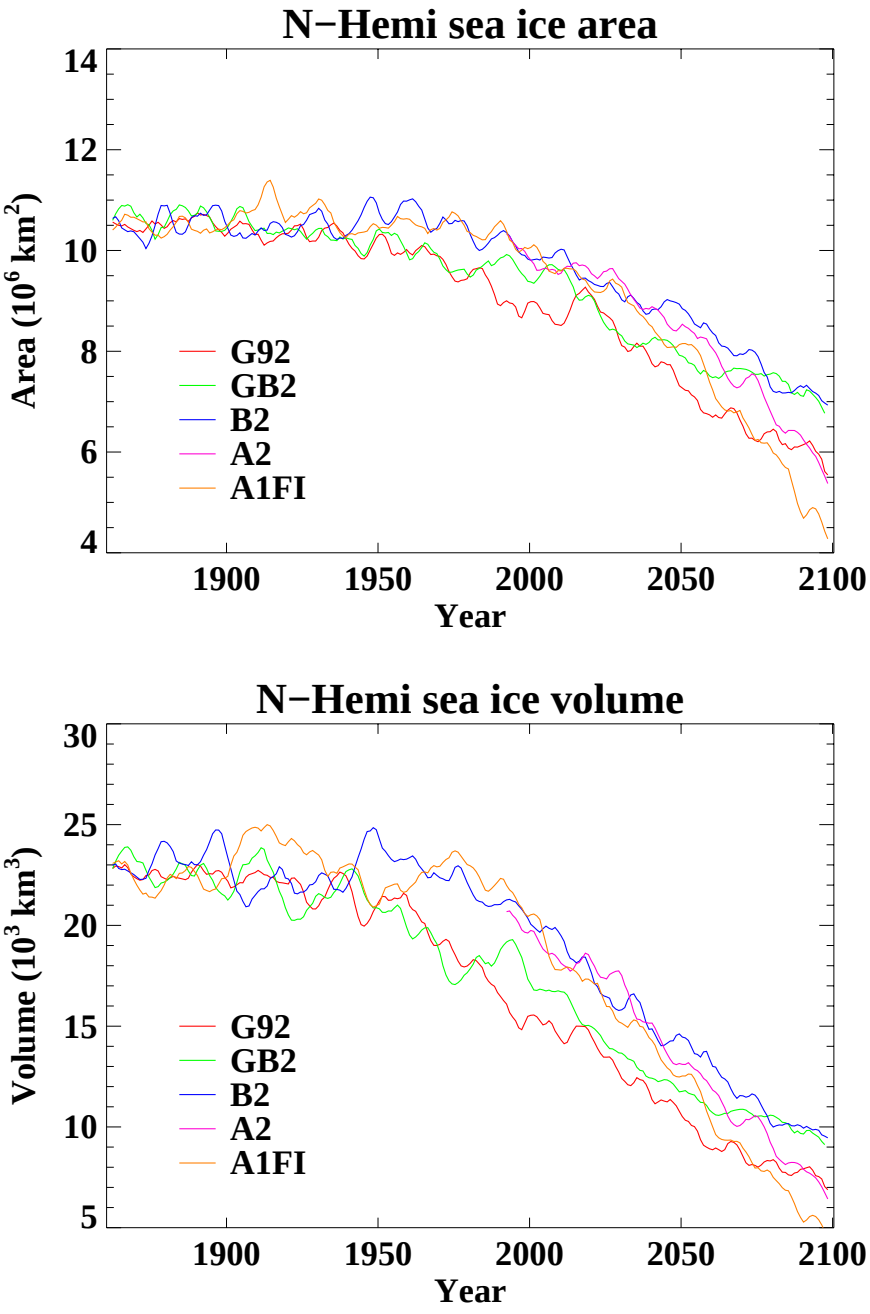

Figure 9: Timeseries of annual mean total sea ice areal coverage and volume in the northern hemisphere (Arctic) in G92, GB2, B2, A2 and A1FI; smoothed using a 5-year running mean.

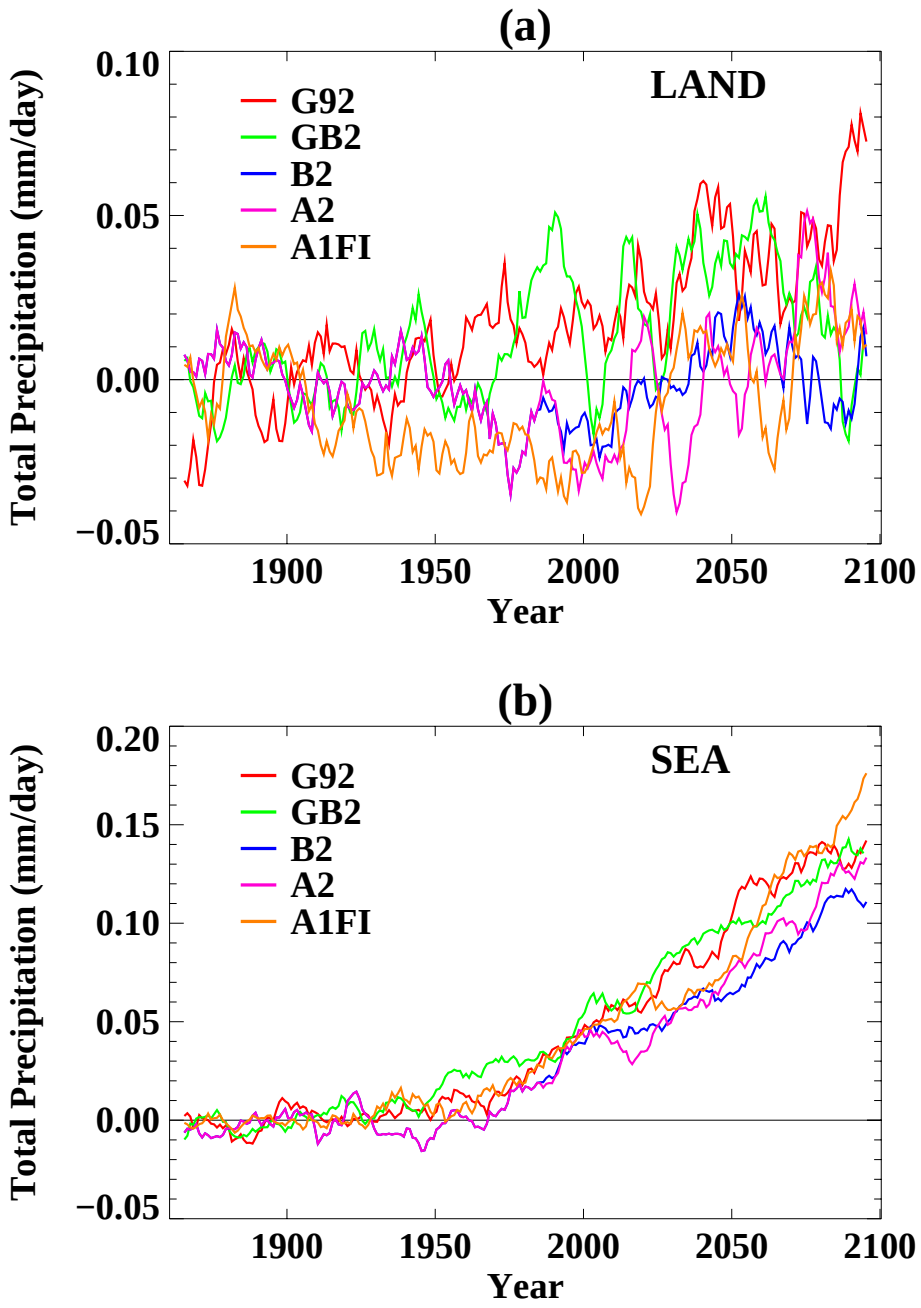

Figure 10: As Figure 7, but for (a) land-only total precipitation and (b) sea-only total precipitation. An 11-year centred mean smoothing has been applied to each curve and observations are not available.

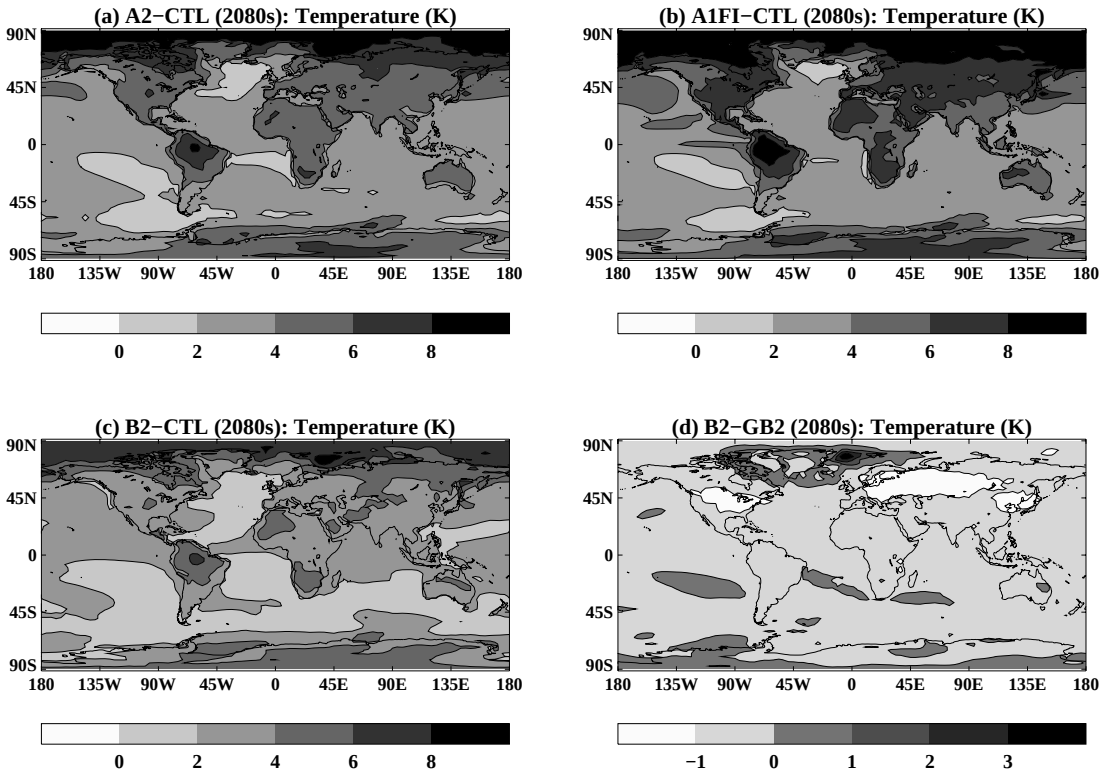

Figure 11: Annual mean changes in surface air temperature (averaged over years 2071-2100) for (a) A2 minus control; (b) A1FI minus control; (c) B2 minus control; and (d) B2 minus GB2. Contours every 1 K in (d), every 2 K otherwise.

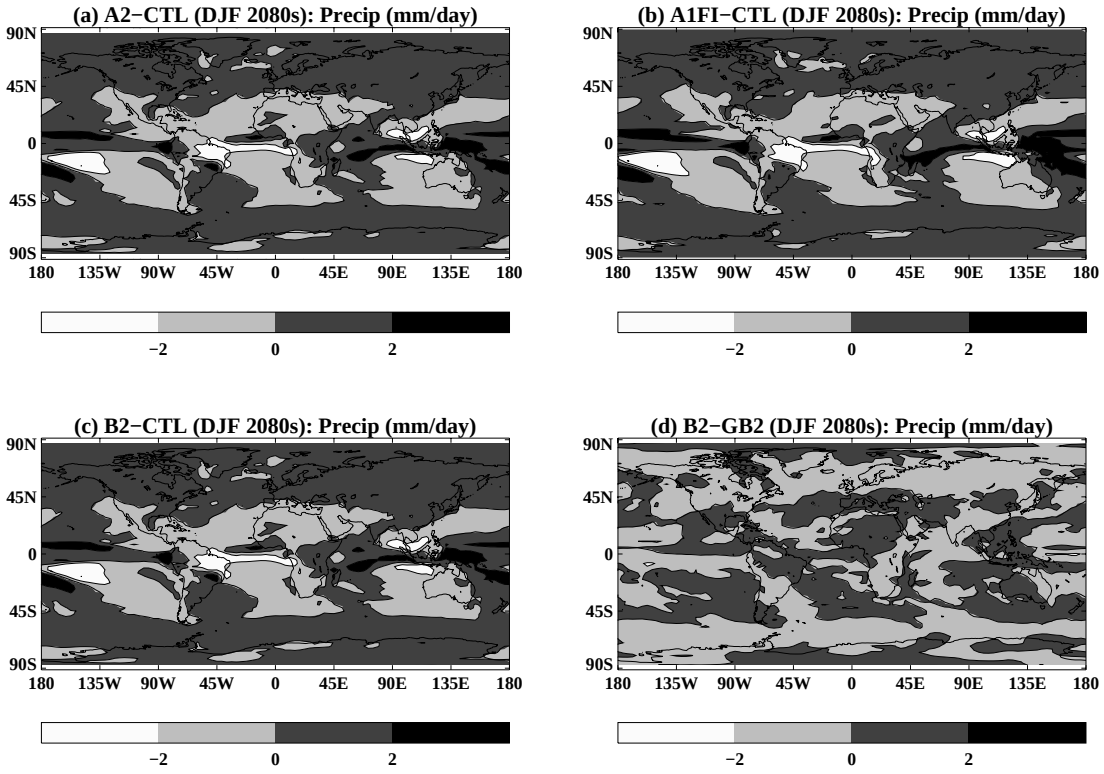

Figure 12: As Figure 11, but for changes in December to February precipitation. Contours every 2 mm/day.

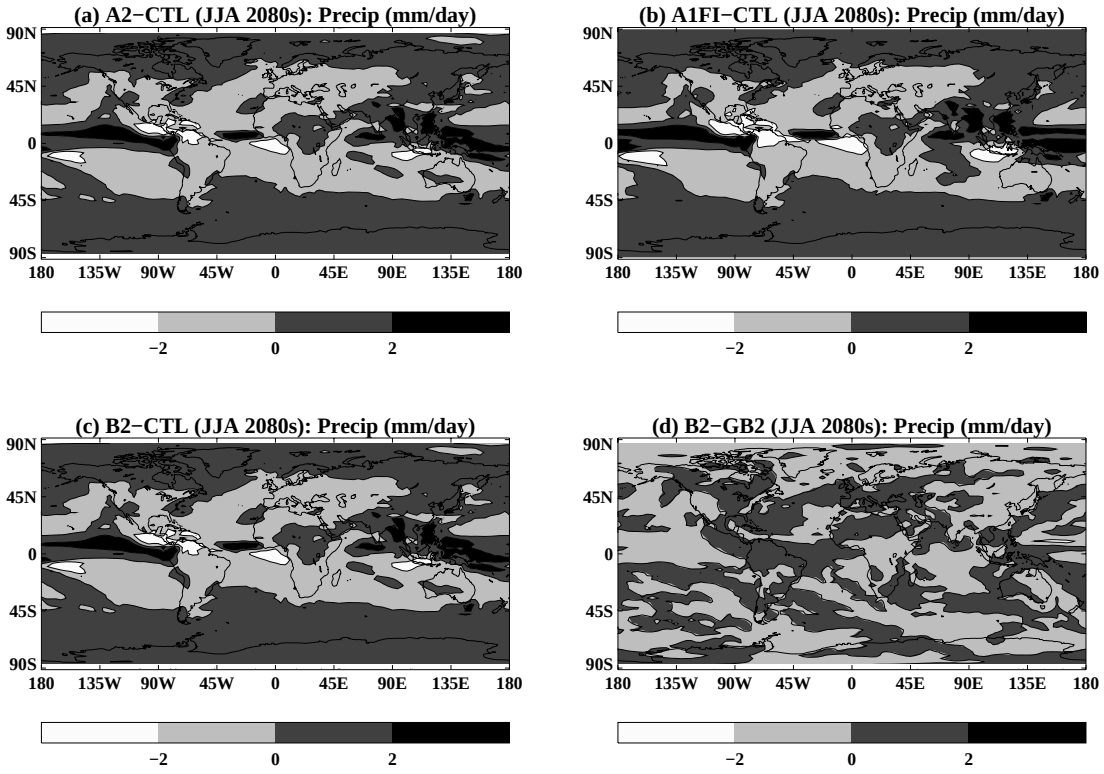

Figure 13: As Figure 12, but for June to August.

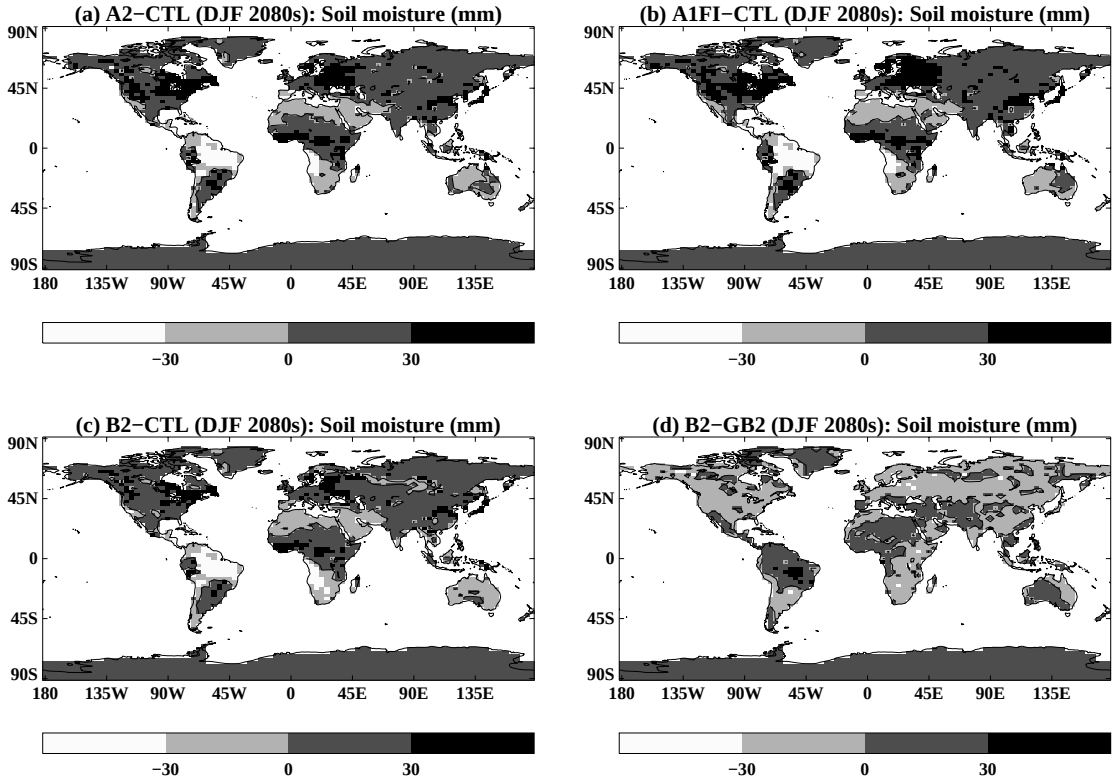

Figure 14: As Figure 12, but for changes in soil moisture content. Contours every 30 mm of water equivalent.

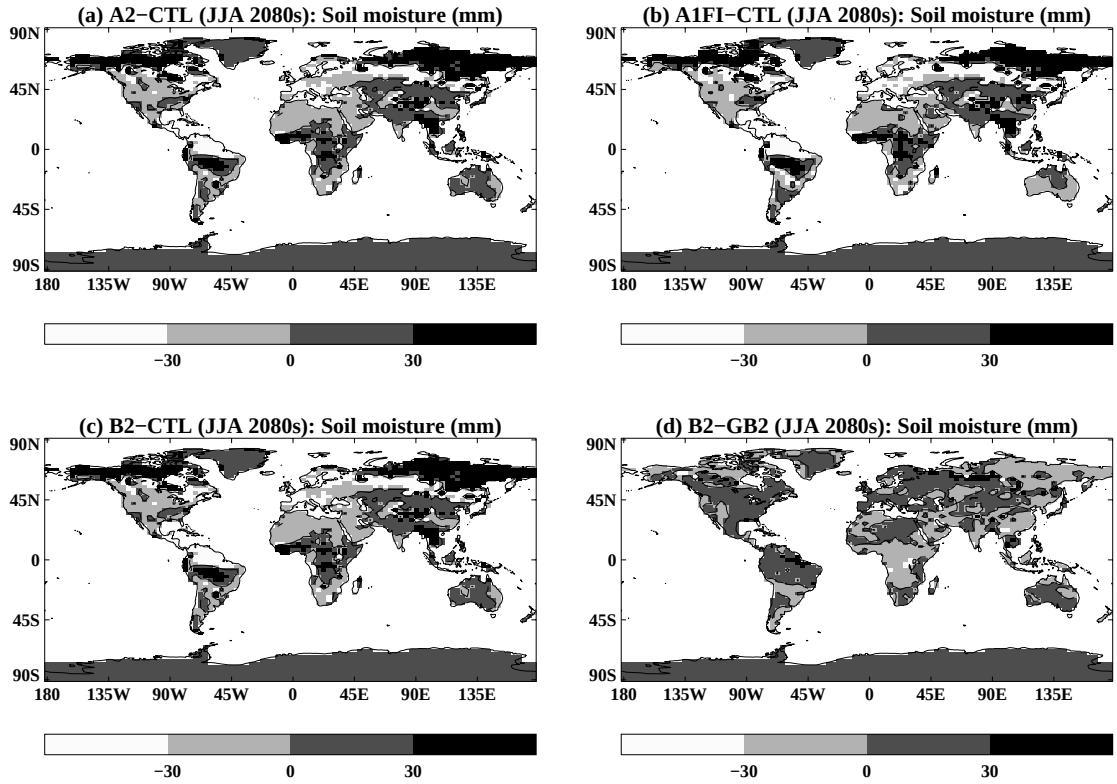

Figure 15: As Figure 14, but for June to August.